Do We Understand Charm and J/ψ Production at RHIC?

R. Vogt

Nuclear Science Division, Lawrence Berkeley National Laboratory, Berkeley, CA 94720, USA

Physics Department, University of California, Davis, CA 95616, USA

The Need for the Charm Quark

Bjorken and Glashow (1964) noted that a fourth quark would lead to more symmetric situation between quarks (up, down and strange) and leptons (e, ν_e, μ, ν_μ)

If only three flavors, there should be strangeness changing neutral currents but they don't exist

Adding a fourth quark would cancel the strangeness changing neutral current (Glashow, Iliopoulos and Maiani, 1970), leaving only $W^- \to d\bar{u}, s\bar{u}, d\bar{c}, s\bar{c}$ and $W^+ \to \bar{d}u, \bar{s}u, \bar{d}c, \bar{s}c$ and no $W^0 \to s\bar{d}$

Renormalizability of triangle anomaly requires the sum of all fermion electric charges to vanish ('t Hooft etc.)

With three flavors: $e_e + e_\mu + 3e_u + 3e_d + 3e_s = -2$

With a fourth flavor: $e_e + e_\mu + 3e_u + 3e_d + 3e_s + 3e_c = 0$

When $\Gamma(K_L^0 \to \mu^+\mu^-)/\Gamma(K_L^0 \to \text{all}) = 9.1 \times 10^{-9}$ is calculated to tune the charm mass, a value of ≈ 1.5 GeV was found (Galliard and Lee)

Charm Mesons

C	Mass (GeV)	$c\tau$ (μm)	$B(C \to lX)$ (%)	$B(C \to$ Hadrons$)$ (%)
$D^+(c\bar{d})$	1.869	315	17.2	$K^-\pi^+\pi^+$ 9.1
$D^-(\bar{c}d)$	1.869	315	17.2	$K^+\pi^-\pi^-$ 9.1
$D^0(c\bar{u})$	1.864	123.4	6.87	$K^-\pi^+$ 3.8
$\overline{D^0}(\bar{c}u)$	1.864	123.4	6.87	$K^+\pi^-$ 3.8
$D^{*\pm}$	2.010			$D^0\pi^\pm$ 67.7, $D^\pm\pi^0$ 30.7
D^{*0}	2.007			$D^0\pi^0$ 61.9
D_1^0	2.420			$D^{*\pm}\pi^\mp$ seen
D_2^{*0}	2.459			$D^\pm\pi^\mp$ seen
$D_2^{*\pm}$	2.459			$D^0\pi^\pm$ seen
$D_s^+(c\bar{s})$	1.969	147	8	$K^+K^-\pi^+$ 4.4, $\pi^+\pi^+\pi^-$ 1.01
$D_s^-(\bar{c}s)$	1.969	147	8	$K^+K^-\pi^-$ 4.4, $\pi^+\pi^-\pi^-$ 1.01
$D_s^{*\pm}$	2.112			$D_s^\pm\gamma$ 94.2
$D_{s1}^\pm$	2.536			$D^{*\pm}K^0$, $D^{*0}K^\pm$ seen

Table 1: Charm mesons with their mass, decay length (when given) and branching ratios to leptons (when applicable) and some prominent decays to hadrons, preferably charged hadrons although such decays are not always available.

Charm Baryons

C	Mass (GeV)	$c\tau$ (μm)	$B(C \to lX)$ (%)	$B(C \to$ Hadrons$)$ (%)
$\Lambda_c^+(udc)$	2.285	59.9	4.5	ΛX 35, $pK^-\pi^+$ 2.8
Λ_c^+	2.593			$\Lambda_c^+\pi^+\pi^-$ 67
Λ_c^+	2.625			$\Lambda_c^+\pi^+\pi^-$ 67
$\Sigma_c^{++}(uuc)$	2.452			$\Lambda_c^+\pi^+$ 100
$\Sigma_c^+(udc)$	2.451			$\Lambda_c^+\pi^0$ 100
$\Sigma_c^0(ddc)$	2.452			$\Lambda_c^+\pi^-$ 100
Σ_c^{++}	2.519			$\Lambda_c^+\pi^+$ 100
Σ_c^+	2.515			$\Lambda_c^+\pi^0$ 100
Σ_c^0	2.518			$\Lambda_c^+\pi^-$ 100
$\Xi_c^+(usc)$	2.466	132		$\Sigma^+K^-\pi^+$ 1.18
$\Xi_c^0(dsc)$	2.472	29		$\Xi^-\pi^+$ seen
$\Xi_c^+(usc)$	2.574			$\Xi_c^+\gamma$ seen
$\Xi_c^0(dsc)$	2.579			$\Xi_c^0\gamma$ seen
$\Omega_c^0(ssc)$	2.698	19		$\Sigma^+K^-K^-\pi^+$, $\Omega^-\pi^+$ seen

Table 2: Charm mesons and baryons with their mass, decay length (when given) and branching ratios to leptons (when applicable) and some prominent decays to hadrons, preferably charged hadrons although such decays are not always available.

Charm Measurements

Two ways to measure charm —

- Directly: observe flight path and decay vertex
- Indirectly: observe decay products and reconstruct mass

Indirect measurements more tricky with large backgrounds but easy in e^+e^-

Observation of decay vertex needed for lifetime studies

Decays to charged particles can be observed in emulsions, bubble chambers, streamer chambers, anywhere a charged particle can leave a trace

Wire chambers and silicon strip counters can measure momentum of charged decay products and allow reconstruction of decays

Experiments Measure Different Parts of Phase Space

Longitudinal momentum fraction, x_F, is a useful observable, $x_F = 2p_L/\sqrt{S} = 2m_T \sinh y/\sqrt{S}$

Bubble chamers cover forward region, $x_F > 0$

Beam dumps measuring either ν or μ

Proton beam dumped onto a dense target which suppresses π and K decays so that, when density is high enough, charm is only remaining lepton source

Extrapolate to infinite density to relate ν and μ flux to the $c\bar{c}$ cross section
Data preferentially at forward x_F, charm not directly reconstructed so momentum is more uncertain

ISR Experiments Are A Special Case

ISR experiments, at $\sqrt{S} = 53 - 63$ GeV, covered small part of phase space so results heavily dependent on extrapolation to full phase space

Some results come from dileptons, others from an electron trigger and a reconstructed charm hadron

Lepton channels ($e^{\pm}\mu^{\mp}$, $e^{+}e^{-}$ and $\mu^{+}\mu^{-}$) give the most reasonable cross sections, $\sigma < 100$ μb

Hadron channel results assumed $pp \rightarrow \overline{D}\Lambda_c X$ and charm x_F distribution can be characterized by $dN/dx_F \sim (1 - x_F)^n$

Used an electron trigger, assumed to be from charm, opposite a reconstructed charm, either $\Lambda_c \rightarrow Kp\pi$ or $D \rightarrow K\pi\pi$
With x_F distribution assumed to go like $n \sim 0$ or $n \sim 3$, $\sigma \geq 500$ μb

Obtaining the Charm Cross Section from Data

Total number of "signal" charm counts determines the minimum bias cross section for the process

$$N_D = \sigma_D L t$$

where Lt is the luminosity over run time

Since

$$\int d^2b T_{AB}(b) = AB$$

Divide by AB to get the per nucleon cross section

Add up all the cross sections for measured D states, D^+, D^0 and their conjugates and correct for the unmeasured part, if coverage is $x_F > 0$, a factor of 1.6 (pions) or 2 (protons) is needed to go to all x_F

$$\sigma_{c\bar{c}} = X \frac{\sigma_{D^+} + \sigma_{D^0} + \sigma_{D^-} + \sigma_{\overline{D^0}}}{2}$$

The factor of two is because the pair cross section is half the sum of the single hadron cross sections

$X = 1.2$ (An Tai) $- 1.5$ (Frixione *et al.*) to account for D_s ($\approx 20\%$) and Λ_c ($\approx 30\%$) production (S. Aoki *et al.*, Prog. Theor. Phys. **87** (1992) 1305)

The A Dependence

A dependence of hard and soft processes are not the same

Total cross section A dependence parameterized as

$$\sigma_{pA} = \sigma_{pp} A^{\alpha}$$

For hard processes, $\alpha \approx 1$, although small nuclear effects like shadowing tend to make $\alpha \neq 1$, albeit close to 1

α may drop with x_F, some indication of this from beam dump experiments

The A dependence of soft processes differs,

$$\alpha(x_F \sim 0) \approx 0.7$$
$$\alpha(x_F \sim 0.8) \approx 0.5$$

Soft behavior is seen for $p \rightarrow \pi, p, K, \Lambda$ with $\alpha = 0.72$ in minimum bias collisions

Hard scattering cross section increases faster with impact parameter than the geometric cross section

Charm is Supposed to Be a 'Hard' Process

'Hard' processes have a large scale in the calculation that makes perturbative QCD applicable: high momentum transfer, μ^2, high mass, m, high transverse momentum, p_T

Understanding these processes relies on asymptotic freedom to calculate the interactions between two hadrons on the quark/gluon level but the confinement scale determines the probability of finding a particular parton in the proton

This implies factorization between the perturbative hard part and the universal, nonperturbative parton distribution functions

$$\sigma_{AB}(S,m^2) = \sum_{i,j=q,\overline{q},g} \int_{4m_Q^2/s}^1 \frac{d\tau}{\tau} \int dx_1\, dx_2\, \delta(x_1 x_2 - \tau) \times f_i^A(x_1,\mu_F^2)\, f_j^B(x_2,\mu_F^2)\, \widehat{\sigma}_{ij}(s,m^2,\mu_F^2,\mu_R^2)$$

f_i^A are the parton distributions, either in a proton or a nucleus, determined from fits to data, x_1 and x_2 are the fractional momentum of the hadron carried by partons i and j, $\tau = s/S$

$\widehat{\sigma}_{ij}(s,m^2,\mu_F^2,\mu_R^2)$ is partonic cross section calculable in QCD in powers of α_s^{2+n}: leading order (LO), $n=0$; next-to-leading order (NLO), $n=1$ ...

Calculating the Total Cross Sections

Partonic total cross section only depends on quark mass m, not kinematic quantitites

To NLO

$$\begin{aligned}\widehat{\sigma}_{ij}(s,m,\mu_F^2,\mu_R^2) &= \frac{\alpha_s^2(\mu_R^2)}{m^2}\left\{ f_{ij}^{(0,0)}(\rho)\right.\\ &+ \left. 4\pi\alpha_s(\mu_R^2)\left[f_{ij}^{(1,0)}(\rho)+f_{ij}^{(1,1)}(\rho)\ln(\mu_F^2/m^2)\right]+O(\alpha_s^2)\right\}\end{aligned}$$

$\rho = 4m^2/s$, s is partonic center of mass energy squared

μ_F is factorization scale, separates hard part from nonperturbative part

μ_R is renormalization scale, scale at which strong coupling constant α_s is evaluated

$\mu_F = \mu_R$ in evaluations of parton densities

$f_{ij}^{(a,b)}$ are dimensionless, μ-independent scaling functions, $a = 0$, $b = 0$ and $ij = q\overline{q}$, gg for LO, $a = 1$, $b = 0, 1$ and $ij = q\overline{q}$, gg and qg, $\overline{q}g$ for NLO

$f_{ij}^{(0,0)}$ are always positive, $f_{ij}^{(1,b)}$ can be negative also

Note that if $\mu_F^2 = m^2$, $f_{ij}^{(1,1)}$ does not contribute

Scaling Functions to NLO

Near threshold, $\sqrt{s}/2m \to 1$, Born contribution is large but dies away for $\sqrt{s}/2m \to \infty$

At large $\sqrt{s}/2m$, gg channel is dominant, then qg

Given high energy behavior of the scaling functions, large changes in the energy dependence of hadronic cross section are difficult to achieve

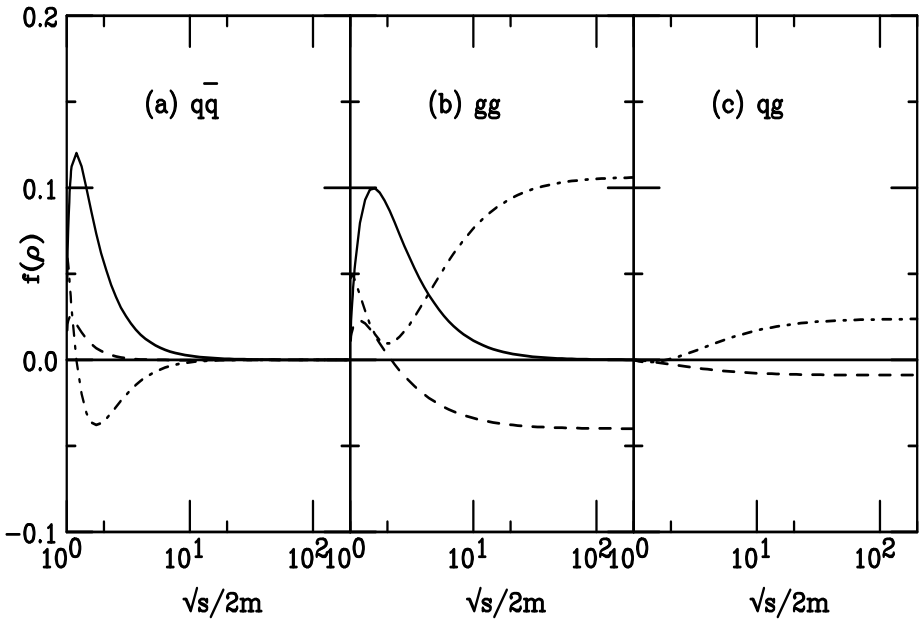

Figure 1: Scaling functions needed to calculate the total partonic $Q\overline{Q}$ cross section. The solid curves are the Born results, $f_{ij}^{(0,0)}$, the dashed and dot-dashed curves are NLO contributions, $f_{ij}^{(1,1)}$ and $f_{ij}^{(1,0)}$ respectively.

Charm Production as a Function of m and μ^2

These calculations keep $\mu_F^2 = \mu_R^2$, as in parton density fits

All pp data from review by Tavernier (1987) as well as more recent data

Data favors lower masses

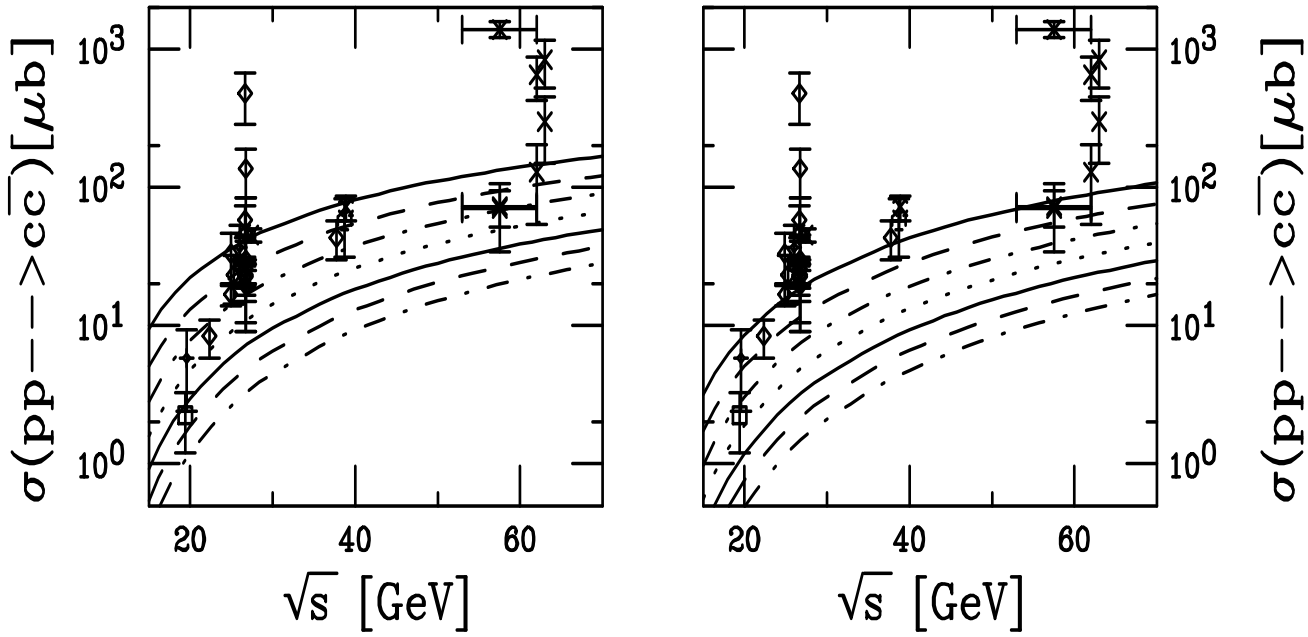

Figure 2: Total $c\bar{c}$ cross sections in pp interactions up to ISR energies as a function of the charm quark mass. All calculations are fully NLO using the MRST HO (central gluon) parton densities. The left-hand plot shows the results with the renormalization and factorization scales equal to m while in the right-hand plot the scale is set to $2m$. From top to bottom the curves are $m = 1.2$, 1.3, 1.4, 1.5, 1.6, 1.7, and 1.8 GeV.

‘Best’ Agreement Found for Several Cases

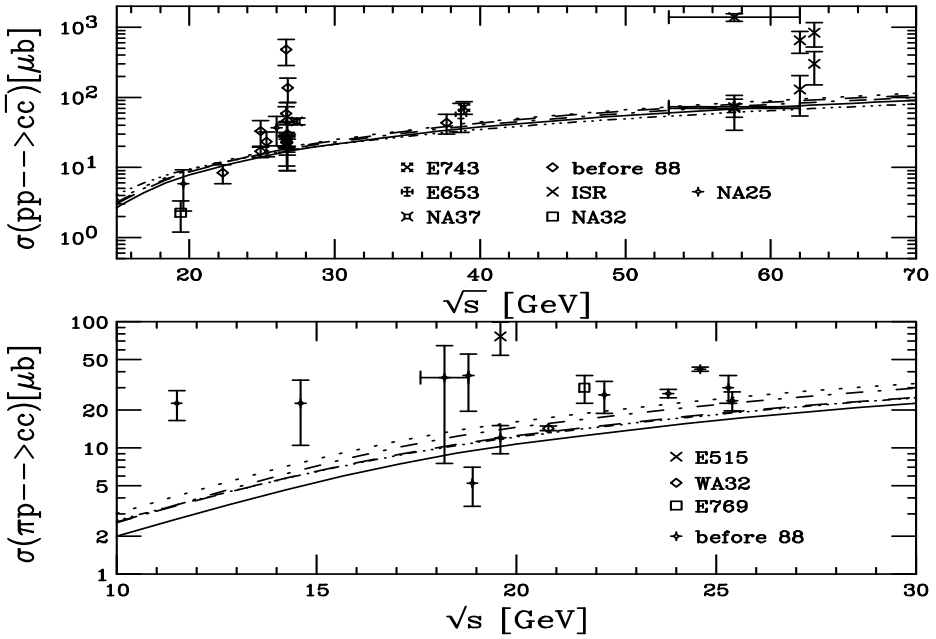

Figure 3: Total $c\bar{c}$ cross sections in pp and $\pi^- p$ interactions compared to data. All calculations are fully NLO. The curves are: MRST HO (central gluon) with $\mu = m = 1.4$ GeV (solid) and $\mu = 2m = 2.4$ GeV (dashed); CTEQ 5M with $\mu = m = 1.4$ GeV (dot-dashed) and $\mu = 2m = 2.4$ GeV (dotted); and GRV98 HO with $\mu = m = 1.3$ GeV.

‘Best’ Extrapolated to Higher Energy

Only two curves remain, MRST HO with $m = 1.2$ GeV, $\mu^2 = 4m^2$ and GRV98 HO with $m = 1.3$ GeV, $\mu^2 = m^2$

We have kept only the most recent measurements, including the PHENIX $\sqrt{S} = 130$ GeV result from Au+Au

The current STAR point lies well above these results

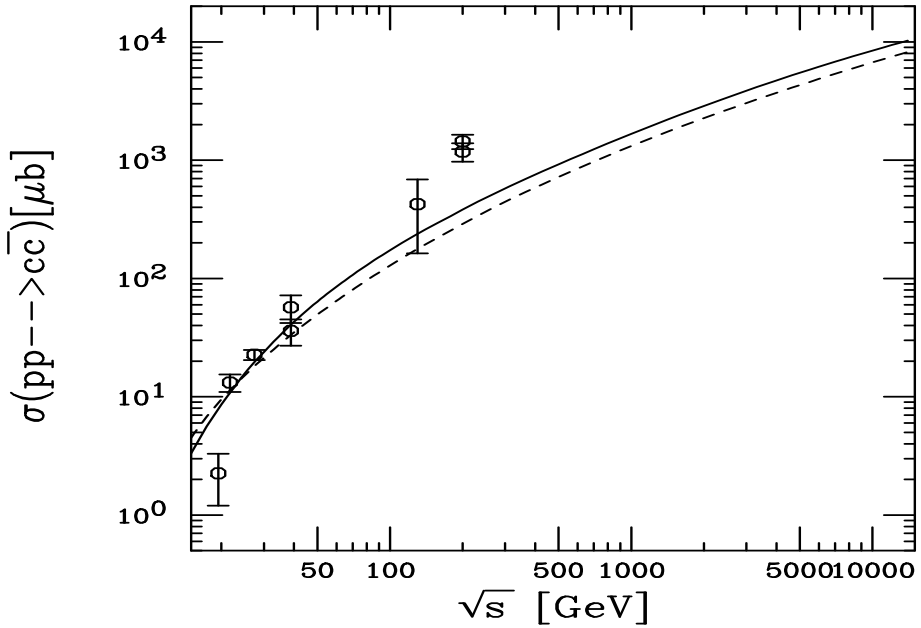

Figure 4: Total $c\bar{c}$ cross sections in pp interactions up to 14 TeV. All calculations are fully NLO. The curves are MRST HO (central gluon) with $m = 1.2$ GeV and $\mu^2 = 4m^2$ (dashed) and GRV98 HO with $m = 1.3$ GeV and $\mu^2 = m^2$.

Can $\sqrt{S}$ Dependence Change? Varying μ_F^2 and μ_R^2

Choose μ_F and μ_R separately so that $\mu_R^2 \leq \mu_F^2$

Going to smaller μ_F does not help, would go below minimum μ^2 for the parton density set

Reducing μ_R^2 increases α_s since $\mu_R^2/\Lambda_{\rm QCD}^2$ gets smaller

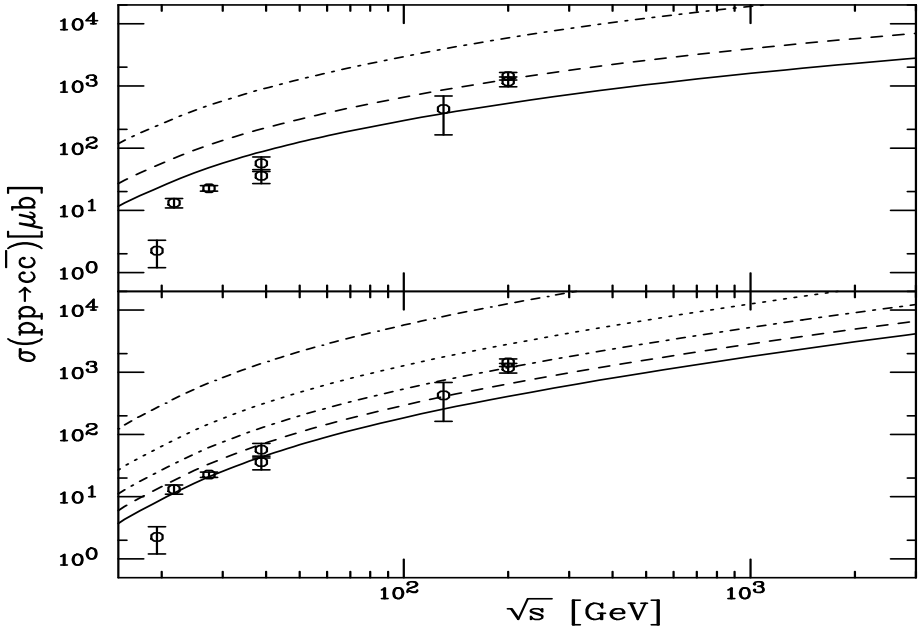

Figure 5: Total $pp \to c\overline{c}$ cross sections calculated for the MRST HO densities with $m = 1.2$ GeV and $\mu_F^2 = m^2$ (upper) and $\mu_F^2 = 4m^2$ (lower). In the upper plot the values of μ_R^2 are m^2 (solid), $m^2/2$ (dashed) and $m^2/4$ (dot dashed). In the lower plot, $\mu_R^2 = 4m^2$ (solid), $2m^2$ (dashed), m^2 (dot-dashed), $m^2/2$ (dotted) and $m^2/4$ (dot-dash-dash-dashed).

Changing μ_F^2 and μ_R^2 Does Not Change Slope

Lower energy data and RHIC data (especially with small error on STAR points) do not lie on same curve

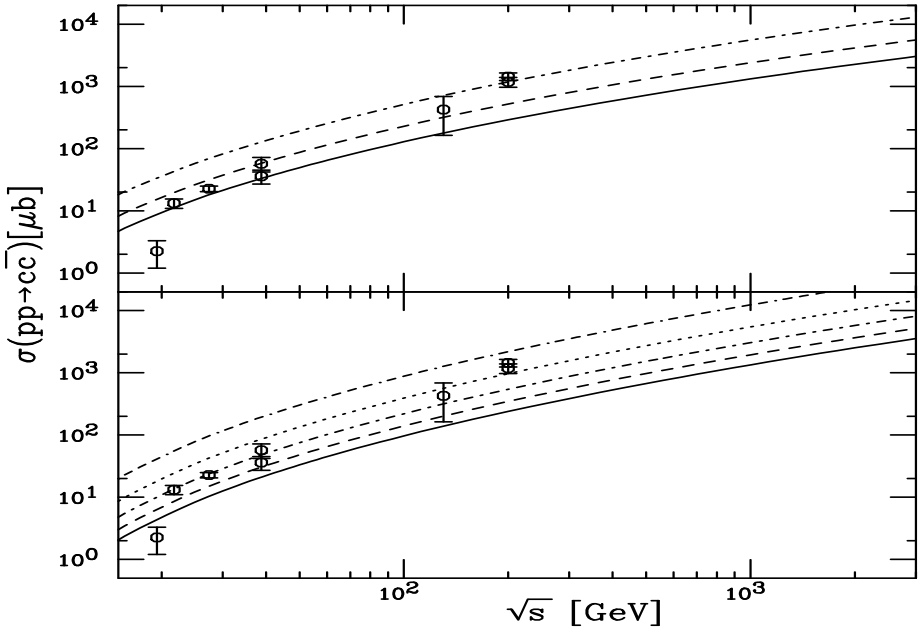

Figure 6: Total $pp \to c\bar{c}$ cross sections calculated for the GRV98 HO densities with $m = 1.3$ GeV and $\mu_F^2 = m^2$ (upper) and $\mu_F^2 = 4m^2$ (lower). In the upper plot the values of μ_R^2 are m^2 (solid), $m^2/2$ (dashed) and $m^2/4$ (dot dashed). In the lower plot, $\mu_R^2 = 4m^2$ (solid), $2m^2$ (dashed), m^2 (dot-dashed), $m^2/2$ (dotted) and $m^2/4$ (dot-dash-dash-dashed).

K Factors Smallest when $\mu_F^2 = \mu_R^2$

The K factor is calculated here as $\sigma_{\rm NLO}/\sigma_{\rm LO}$ with both numerator and denominator calculated with NLO parton densities and two-loop α_s

K factor larger for MRST HO when $\mu_F^2 = m^2$, close to minimum μ^2 for these densities

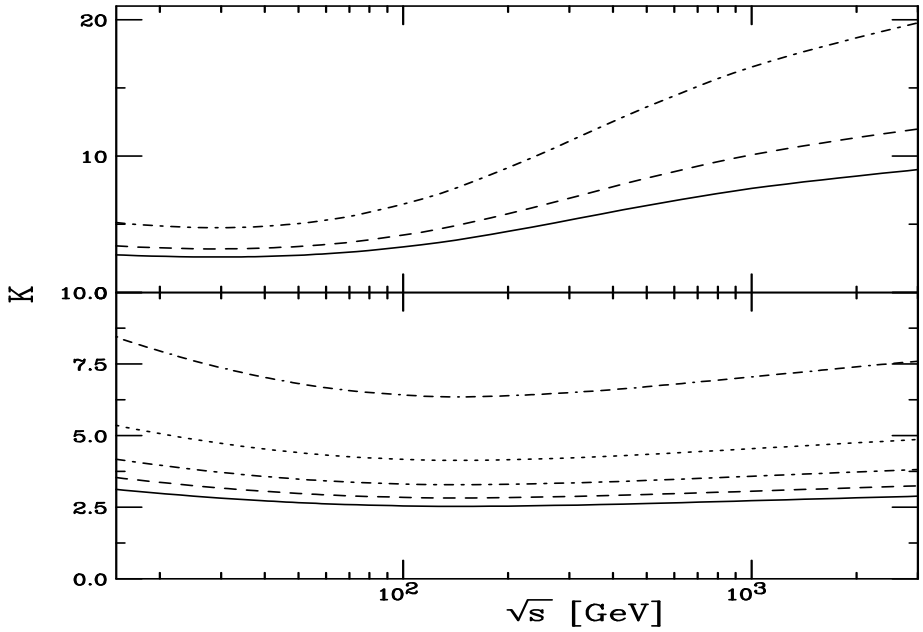

Figure 7: The $c\bar{c}$ K factors in pp interactions calculated using the MRST HO densities, $m = 1.2$ GeV and $\mu_F^2 = m^2$ (upper) and $\mu_F^2 = 4m^2$ (lower). In the upper plot the values of μ_R^2 are m^2 (solid), $m^2/2$ (dashed) and $m^2/4$ (dot dashed). In the lower plot, $\mu_R^2 = 4m^2$ (solid), $2m^2$ (dashed), m^2 (dot-dashed), $m^2/2$ (dotted) and $m^2/4$ (dot-dash-dash-dashed).

GRV98 HO K Factors Smaller

For these densities, $\mu_F^2 = m^2 > \mu_{\rm min}^2$ so corrections do not become so large

K factors are a measure of stability and convergence of perturbative expansion

K is large, > 2, so next order corrections will still be important

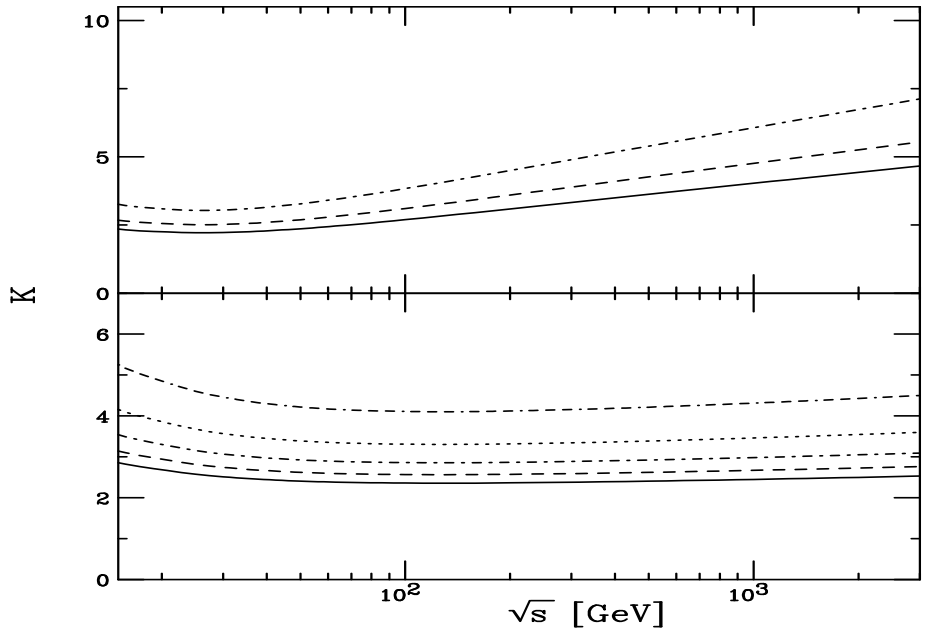

Figure 8: The $c\bar{c}$ K factors in pp interactions calculated using the GRV98 HO densities, $m = 1.3$ GeV and $\mu_F^2 = m^2$ (upper) and $\mu_F^2 = 4m^2$ (lower). In the upper plot the values of μ_R^2 are m^2 (solid), $m^2/2$ (dashed) and $m^2/4$ (dot dashed). In the lower plot, $\mu_R^2 = 4m^2$ (solid), $2m^2$ (dashed), m^2 (dot-dashed), $m^2/2$ (dotted) and $m^2/4$ (dot-dash-dash-dashed).

Try Alternative Way to Calculate NLO

Inclusive charm hadroproduction cross section

$$d\sigma_{pp\to c\bar{c}X}(\sqrt{s},m,\mu_R^2,\mu_F^2)\sum_{i,j=q,\bar{q},g} f_i(x_1,\mu_F^2)\otimes f_j(x_2,\mu_F^2)\otimes d\hat{\sigma}_{ij\to c\bar{c}\{k\}}(\alpha_s(\mu_R^2),\mu_F^2,m,x_1,x_2)$$

$k=0$ at LO and 0, q, $\bar{q}$ or g at NLO

NLO cross section can be calculated in two ways:

- "standard NLO" — NLO PDFs and two-loop α_s at each order

$$\begin{aligned} d\sigma_{\rm NLO}^{\rm std} &= \sum_{i,j=q,\bar{q},g} f_i^{\rm NLO}(x_1,\mu_F^2)\otimes f_j^{\rm NLO}(x_2,\mu_F^2)\otimes d\hat{\sigma}_{ij\to c\bar{c}}^{\rm LO}(\alpha_s^{\rm 2L}(\mu_R^2),x_1,x_2) \\ &+ \sum_{i,j=q,\bar{q},g} f_i^{\rm NLO}(x_1,\mu_F^2)\otimes f_j^{\rm NLO}(x_2,\mu_F^2)\otimes \sum_{k=0,q,\bar{q},g} d\hat{\sigma}_{ij\to c\bar{c}k}^{\rm NLO}(\alpha_s^{\rm 2L}(\mu_R^2),\mu_F^2,x_1,x_2) \\ &\equiv d\sigma_{\rm LO}^{\rm 2L}+d\sigma_{O(\alpha_s^3)} \end{aligned}$$

- "alternative NLO" — LO PDFs and one-loop α_s for LO part, NLO PDFs and two-loop α_s for NLO contribution

$$\begin{aligned} d\sigma_{\rm NLO}^{\rm alt} &= \sum_{i,j=q,\bar{q},g} f_i^{\rm LO}(x_1,\mu_F^2)\otimes f_j^{\rm LO}(x_2,\mu_F^2)\otimes d\hat{\sigma}_{ij\to c\bar{c}}^{\rm LO}(\alpha_s^{\rm 1L}(\mu_R^2),x_1,x_2) \\ &+ \sum_{i,j=q,\bar{q},g} f_i^{\rm NLO}(x_1,\mu_F^2)\otimes f_j^{\rm NLO}(x_2,\mu_F^2)\otimes \sum_{k=0,q,\bar{q},g} d\hat{\sigma}_{ij\to c\bar{c}k}^{\rm NLO}(\alpha_s^{\rm 2L}(\mu_R^2),\mu_F^2,x_1,x_2) \\ &\equiv d\sigma_{\rm LO}^{\rm 1L}+d\sigma_{O(\alpha_s^3)} \end{aligned}$$

Alternative NLO Increases Cross Section at High $\sqrt{S}$

$\sigma^{\rm alt}_{\rm NLO} > \sigma^{\rm std}_{\rm NLO}$ at large $\sqrt{S}$ because some NLO gluon distribution can become small or negative at low x

Effect is not large enough to make a significant change in $\sqrt{S}$ dependence at RHIC

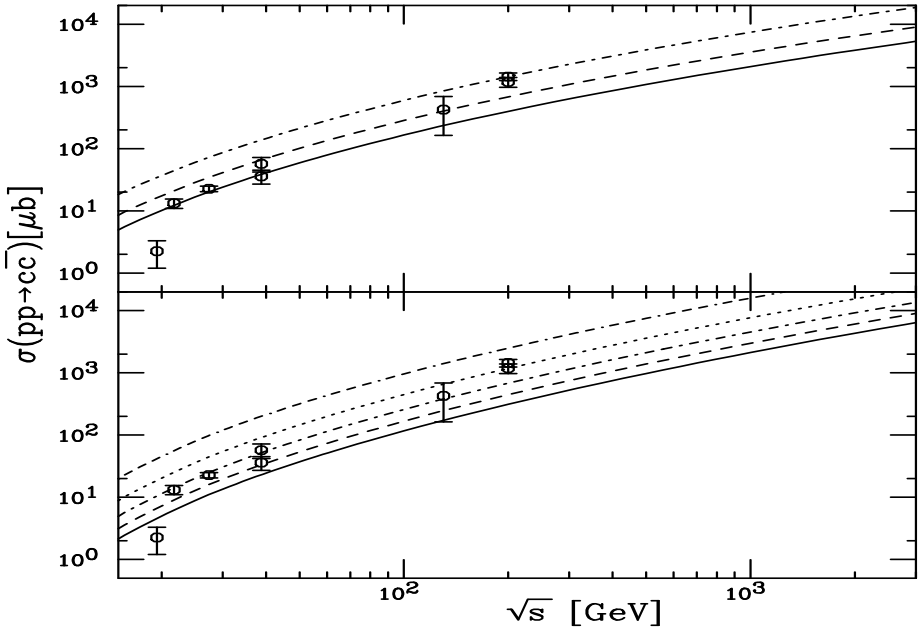

Figure 9: Total $pp \to c\bar{c}$ cross sections calculated using the alternative NLO result. The cross sections are obtained for the GRV98 HO densities with $m = 1.3$ GeV and $\mu_F^2 = m^2$ (upper) and $\mu_F^2 = 4m^2$ (lower). In the upper plot the values of μ_R^2 are m^2 (solid), $m^2/2$ (dashed) and $m^2/4$ (dot dashed). In the lower plot, $\mu_R^2 = 4m^2$ (solid), $2m^2$ (dashed), m^2 (dot-dashed), $m^2/2$ (dotted) and $m^2/4$ (dot-dash-dash-dashed).

Uusing $\sigma^{\rm alt}_{\rm NLO}$ Reduces K

Energy dependence of K factor defined as $\sigma^{\rm alt}_{\rm NLO}/\sigma^{\rm 1L}_{\rm LO}$ is reduced, especially at high $\sqrt{S}$

At fixed target energies, $\sigma^{\rm alt}_{\rm NLO}$ and $\sigma^{\rm std}_{\rm NLO}$ differ by only the values of one- and two-loop α_s ($\alpha_s^{\rm 1L} > \alpha_s^{\rm 2L}$) since LO and NLO gluon densities are similar at large x

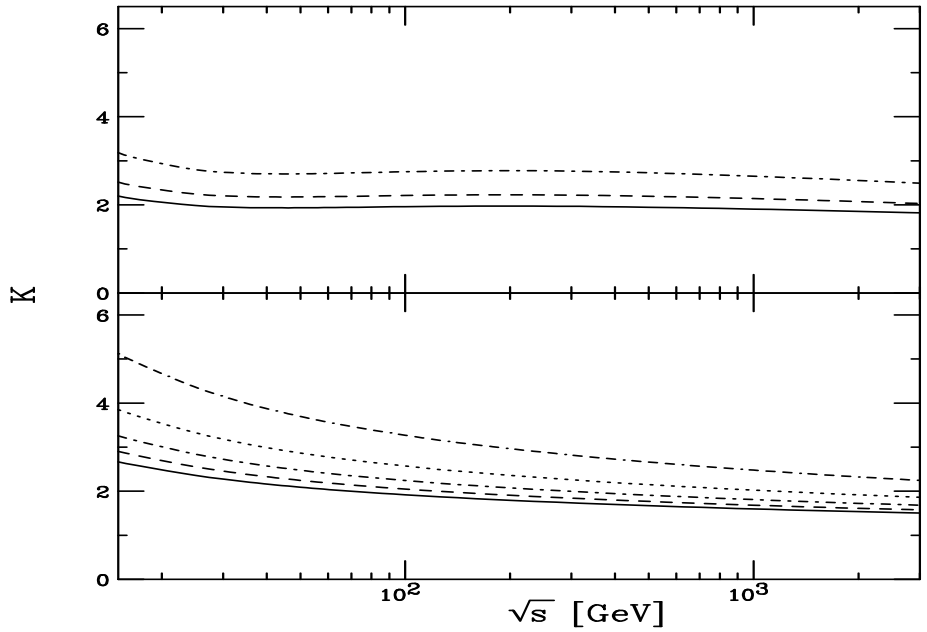

Figure 10: The $c\bar{c}$ K factors in pp interactions calculated using the alternative NLO cross sections with the GRV98 HO densities, $m = 1.3$ GeV and $\mu_F^2 = m^2$ (upper) and $\mu_F^2 = 4m^2$ (lower). In the upper plot the values of μ_R^2 are m^2 (solid), $m^2/2$ (dashed) and $m^2/4$ (dot dashed). In the lower plot, $\mu_R^2 = 4m^2$ (solid), $2m^2$ (dashed), m^2 (dot-dashed), $m^2/2$ (dotted) and $m^2/4$ (dot-dash-dash-dashed).

From Total Cross Sections to Distributions

In total cross section, the quark mass is the only relevant scale

When considering kinematical observables like x_F or p_T, the momentum scale is also relevant so that, instead of $\mu^2 \propto m^2$, one usually uses $\mu^2 \propto m_T^2$

Other important considerations for distributions: fragmentation and intrinsic k_T

Fragmentation assumed to be universal, like parton densities, so the parameterizations of e^+e^- data (*e.g.* Peterson function) should work in hadroproduction
Effect of intrinsic transverse momentum broadening decreases with energy

Effects of Fragmentation and Intrinsic k_T on Distributions

Double differential cross sctions

$$s^2 \frac{d^2\sigma_{pp}(s,t,u)}{dtdu} = \sum_{i,j=q,\overline{q},g} \int_{x_1^-}^1 \frac{dx_1}{x_1} \int_{x_2^-}^1 \frac{dx_2}{x_2} f_i^p(x_1,\mu^2) f_j^p(x_2,\mu^2) \jmath_K(\hat{s},\hat{t},\hat{u}) \hat{s}^2 \frac{d^2\hat{\sigma}_{ij}(\hat{s},\hat{t},\hat{u})}{d\hat{t}d\hat{u}}$$

$f_i^p = F_i^p/x$ is parton density, $\jmath_K$ is a kinematics-dependent Jacobian

Intrinsic transverse momentum and fragmentation are needed to smear the pair p_T and ϕ distributions as measured for $D\overline{D}$ correlations (Peterson fragmentation and $k_T^2 = 1$ GeV^2 cancel each other in low $\sqrt{S}$ single D p_T distributions)

Adds the following extra integrations:

$$\int dz_3 dz_4 d^2k_{T1} d^2k_{T2} \frac{D_{H/Q}(z_3,\mu^2)}{z_3} \frac{D_{\overline{H}/\overline{Q}}(z_4,\mu^2)}{z_4} g_p(k_{T1}) g_p(k_{T2})$$

Fragmentation function a la Peterson

$$D_{H/Q}(z) = \frac{N}{z(1-1/z-\varepsilon_Q/(1-z))^2}$$

$\varepsilon_Q = 0.06$ for charm, 0.006 for bottom, normalized so that $\sum_H \int D_{H/Q}(z)dz = 1$ for all heavy flavored hadrons

Gaussian k_T smearing, $\langle k_T^2 \rangle = 1$ GeV^2 for pp, broadened for pA and AA, added in final state in NLO code

$$g_p(k_T) = \frac{1}{\pi \langle k_T^2 \rangle_p} \exp(-k_T^2/\langle k_T^2 \rangle_p) \quad (1)$$

Bare Quark Distribution Works Better for x_F

$x_F = 2p_L/\sqrt{S} = 2m_T \sinh y/\sqrt{S}$ distributions integrated over p_T, average goes into m_T in x_F

$pp \to DX$ at 400 GeV, fixed target shown here

Bare distribution (delta function) works better than the Peterson function (dashed curve) which falls below data

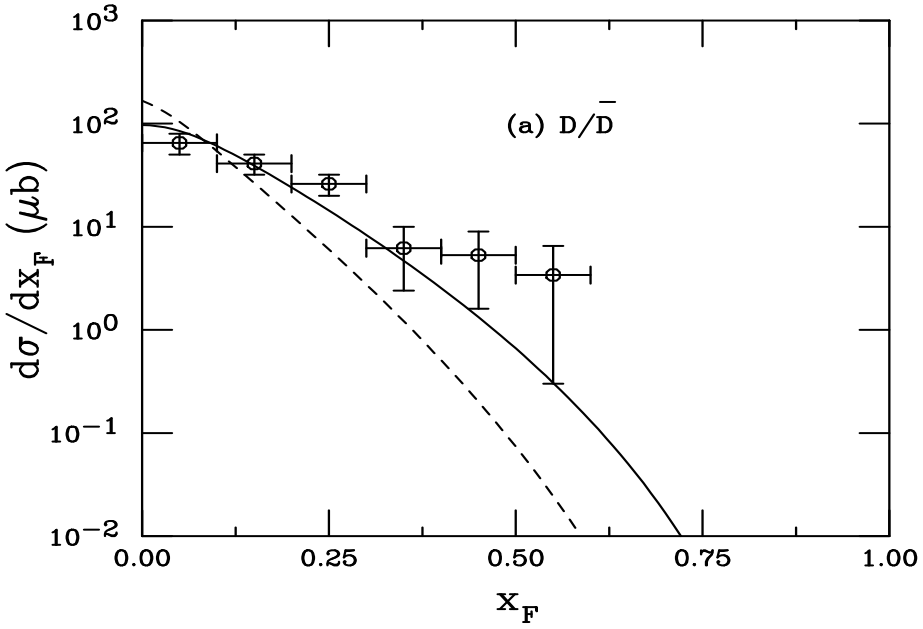

Figure 11: Comparison of calculations with data from 400 GeV pp interactions. The dashed curve uses the Peterson function while the solid curve is a delta function. The data are from M. Aguilar-Benitez *et al.*, Phys. Lett. **B189**, 476 (1987), the calculations from R.V. *et al.*, Nucl. Phys. **B383**, 643 (1992).

Cancelation of Fragmentation and k_T at $\sqrt{S} = 16$ GeV

Bare charm (solid) and Peterson fragmentation with $\langle k_T^2 \rangle = 1$ GeV^2 (dotted) on top of each other

Broadening alone, $\langle k_T^2 \rangle = 1$ GeV^2, widens p_T distribution

Peterson fragmentation alone (dot-dashed) below bare

Large $\langle k_T^2 \rangle$ (dot-dot-dot-dashed) in between

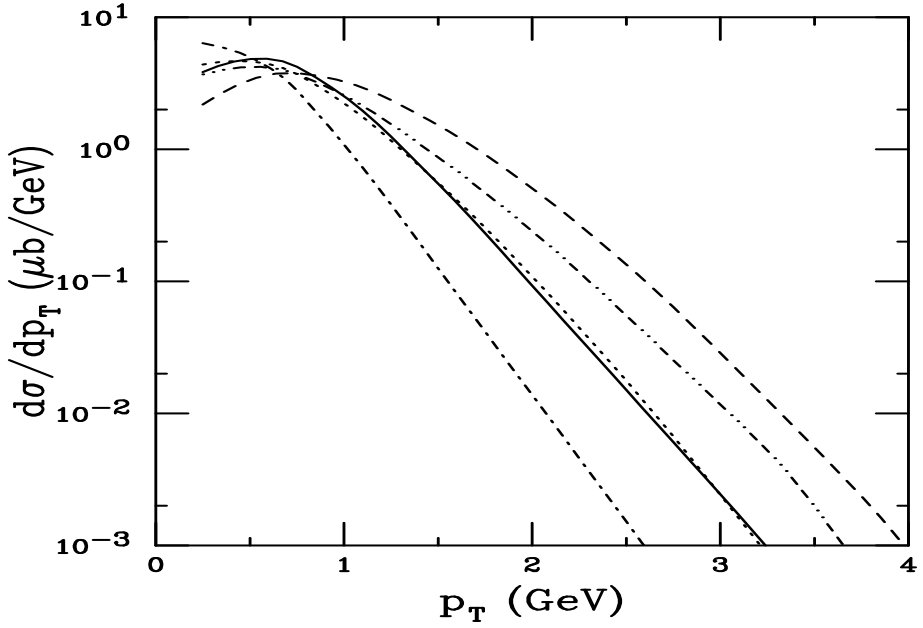

Figure 12: For a fixed-target experiment with $p_{\rm lab} = 158$ GeV, we compare the NLO p_T distributions including fragmentation and intrinsic k_T. The solid curves shows the bare distribution, the dashed includes $\langle k_T^2 \rangle = 1$ GeV^2 but no fragmentation, the dot-dashed is Peterson fragmentation alone, the dotted and dot-dot-dot-dashed include both Peterson fragmentation and broadening with $\langle k_T^2 \rangle = 1$ and 1.7 GeV^2 respectively.

No Cancelation at RHIC

$\langle k_T^2 \rangle = 1$ GeV^2 alone (dashed) is now a small effect since $\langle p_T \rangle$ is much larger than at fixed-target energies

Peterson fragmentation alone (dot-dashed) below bare distribution, going to higher $\langle k_T^2 \rangle$ does not help, 1.7 GeV^2 is largest shown, even 4 GeV^2 does not bring the result closer to the bare distribution

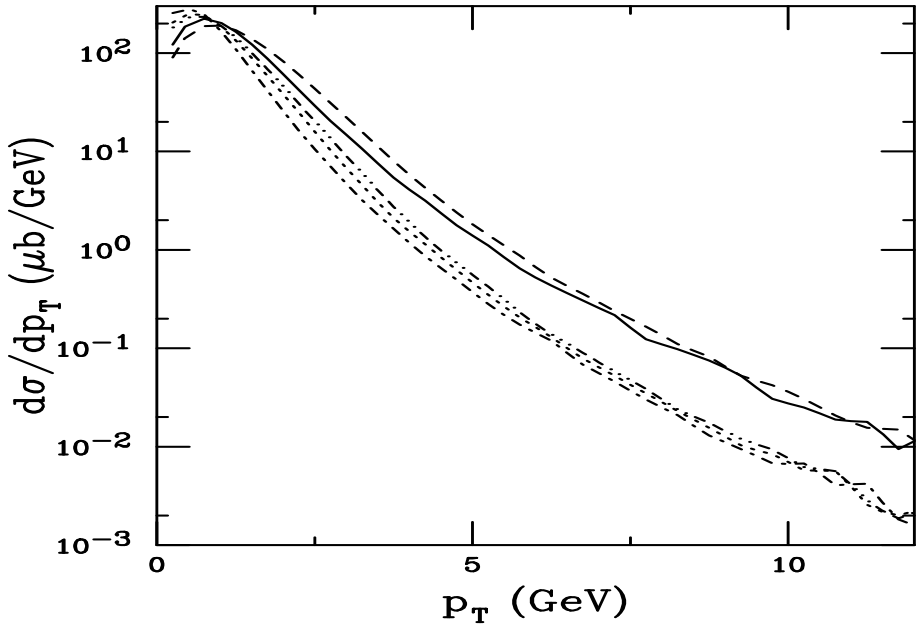

Figure 13: We compare the NLO p_T distributions including fragmentation and intrinsic k_T at $\sqrt{S_{NN}} = 200$ GeV. The solid curves shows the bare distribution, the dashed includes $\langle k_T^2 \rangle = 1$ GeV^2 but no fragmentation, the dot-dashed is Peterson fragmentation alone, the dotted and dot-dot-dot-dashed include both Peterson fragmentation and broadening with $\langle k_T^2 \rangle = 1$ and 1.7 GeV^2 respectively.

Other Models of Heavy Quark p_T Distributions

FONLL scheme designed to cure logs of p_T/m for $p_T \gg m$ in the p_T distributions

Adds subset of NLL exponents with equivalent NLO terms subtracted out

Comparing the bare distributions at $\sqrt{S} = 200$ GeV and the same parameters as the NLO calculation, we see that the slopes are similar at high p_T but flatter at low p_T, giving a lower total cross section

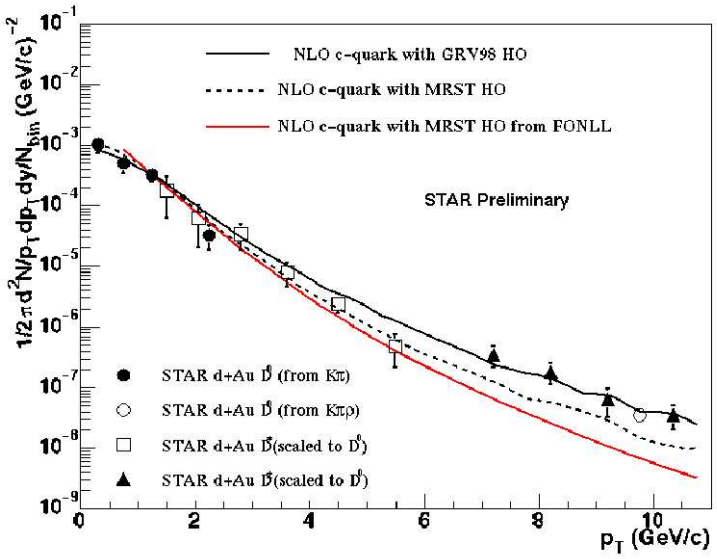

Figure 14: The STAR *D* meson data is compared to NLO and FONLL bare charm calculations. The black curve shows the NLO calculation with the GRV98 HO parton densites, $m = 1.3$ GeV and $\mu = m_T$ while the dotted curve is the NLO result with MRST HO parton densities, $m = 1.2$ GeV and $\mu = 2m_T$. The red curve is the FONLL calculation with the same parameters as the dotted curve. All curves are scaled to fi t the data. [FONLL calculation by A. Tai (STAR).]

Comparison of STAR and CDF x_T Distributions

To better compare RHIC and Tevatron results, the $x_T = 2p_T/\sqrt{S}$ distributions are constructed for both charm and charged hadron distributions

CDF and STAR D slopes are similar for STAR $p_T > 3$ GeV

CDF x_T distributions shifted to smaller x_T by $\sqrt{S_{\rm STAR}}/\sqrt{S_{\rm CDF}} \sim 0.1$

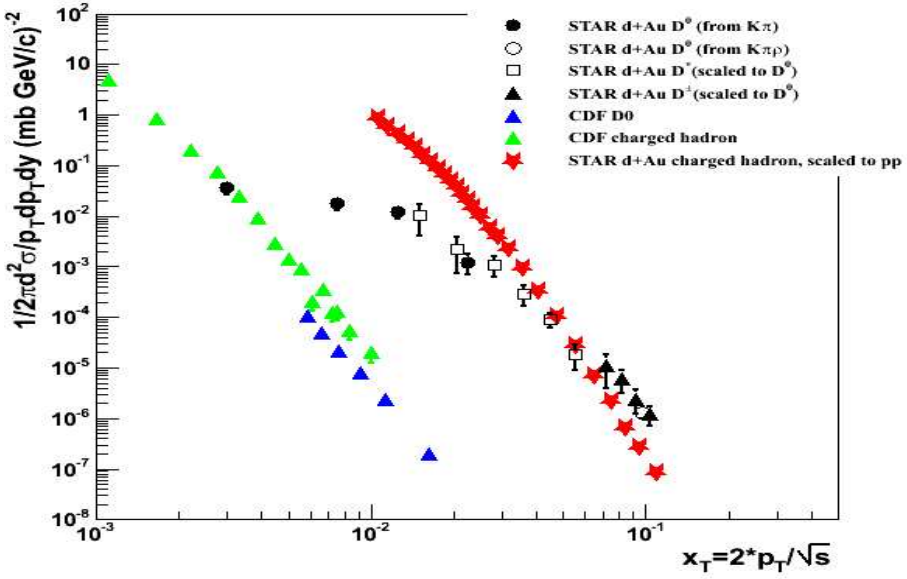

Figure 15: Comparison of STAR ($\sqrt{S_{NN}} = 200$ GeV) and CDF ($\sqrt{S} = 1960$ GeV) x_T distributions for D mesons and charged hadrons. [Plot courtesy of An Tai (STAR).]

CDF Data Agrees with NLO Charm Distribution

CDF data shown are sum of D^+ and D^0 (and conjugate) distributions, error bars are convolution of statistical and systematic errors

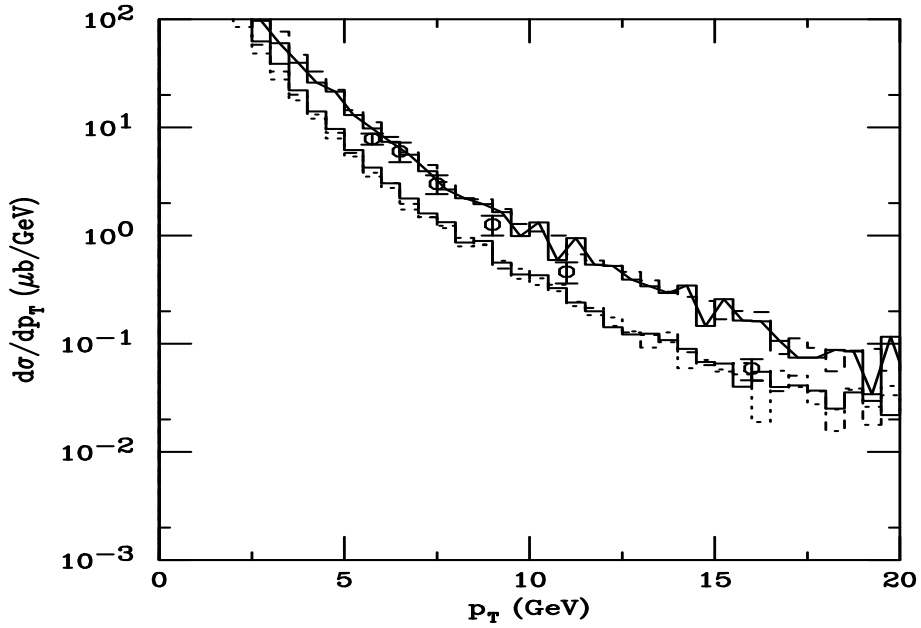

Figure 16: We compare the NLO p_T distributions including fragmentation and intrinsic k_T at $\sqrt{S_{NN}} = 200$ GeV. The upper solid histogram and curve shows the bare distribution, the dashed includes $\langle k_T^2 \rangle = 1$ GeV^2 but no fragmentation, the dot-dashed is Peterson fragmentation alone, the dotted and lower solid include both Peterson fragmentation and broadening with $\langle k_T^2 \rangle = 1$ and 1.7 GeV^2 respectively.

Charm Not Produced at Very Low x at RHIC

Compare μ^2 and x at several values of charm quark rapidity when rapidity of unobserved c (or $\bar{c}$) integrated away, $m = 1.2$ GeV, $\mu^2 = 4m_T^2$

$x_2 = (2m_T/\sqrt{S})(\exp(-y) + \exp(-y_2)) \geq 0.01$ at LO, not symmetric around $y = 0$

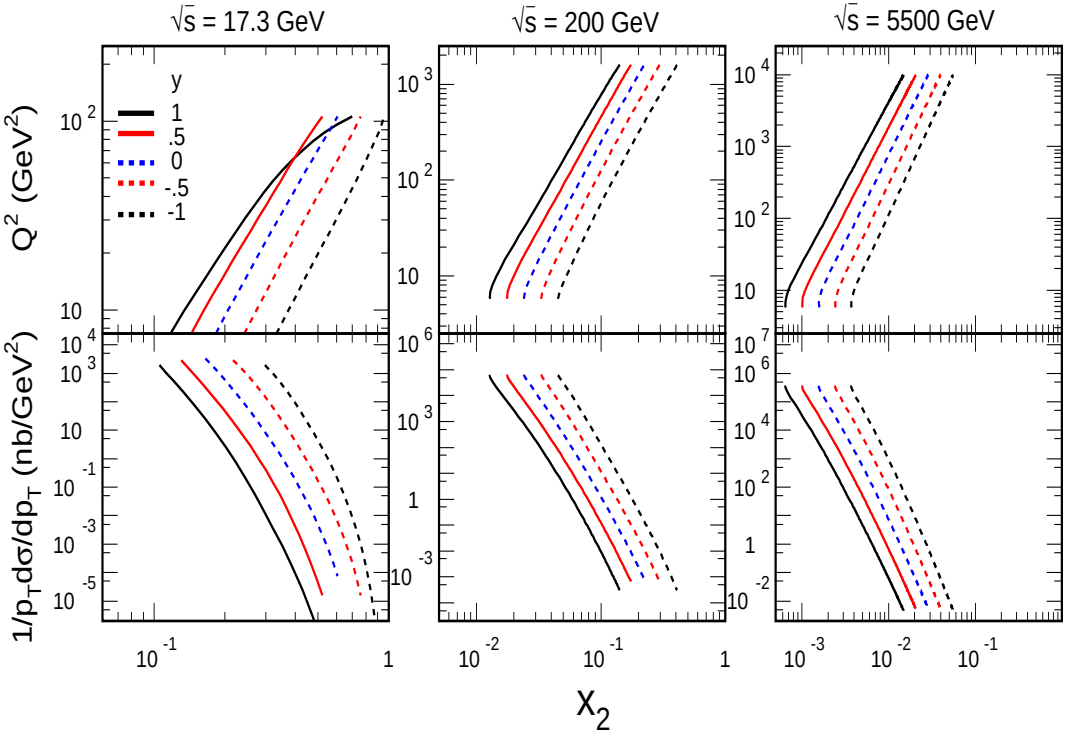

Figure 17: Curves of Q^2 (upper) and $d\sigma/p_T dp_T$ as a function of x_2 for $y = 1$, 0.5, 0, -0.5 and -1 when the rapidity of the unobserved quark is integrated away. (With N. Xu and L. Grandchamp.)

Influence on J/ψ of Large $\sigma_{c\bar{c}}$

Regeneration of J/ψ possible when more than 1 $c\bar{c}$ pair produced per event

$\sigma_{c\bar{c}} \approx 0.35$ mb from pQCD, about 8 $c\bar{c}$ pairs/event

Preliminary STAR cross section, 1.1 – 1.4 mb, 26 – 33 $c\bar{c}$/event, increasing J/ψ yield per collision

Increase inconsistent with PHENIX Au+Au data, PHENIX pp result more consistent with pQCD

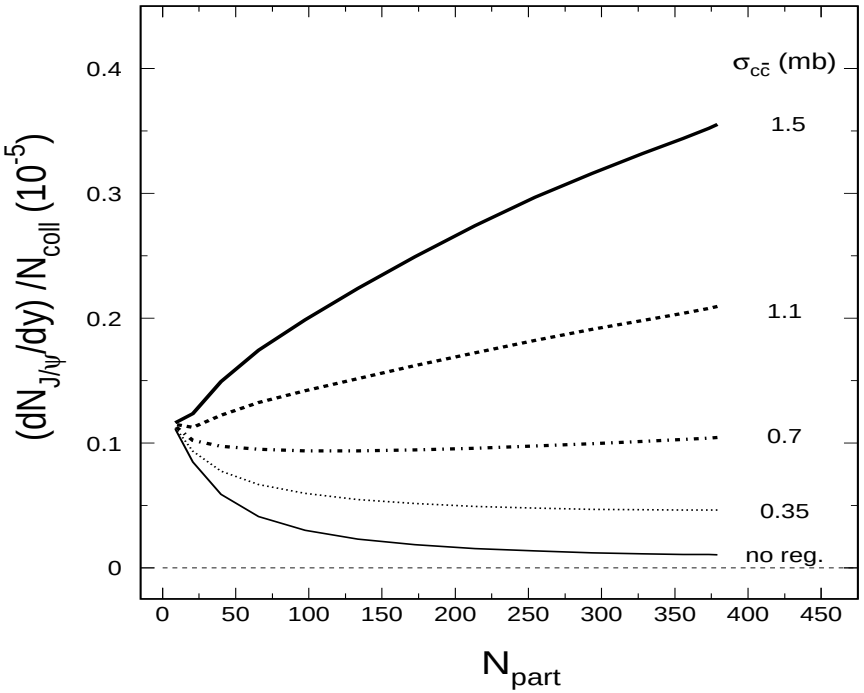

Figure 18: The effect of various values of the $c\bar{c}$ total cross section on the number of J/ψ produced per binary collision as a function of the number of participants. (With N. Xu and L. Grandchamp.)

PHENIX J/ψ pp Rapidity Distribution Close to that from pQCD

No scaling needed to obtain reasonable agreement with data

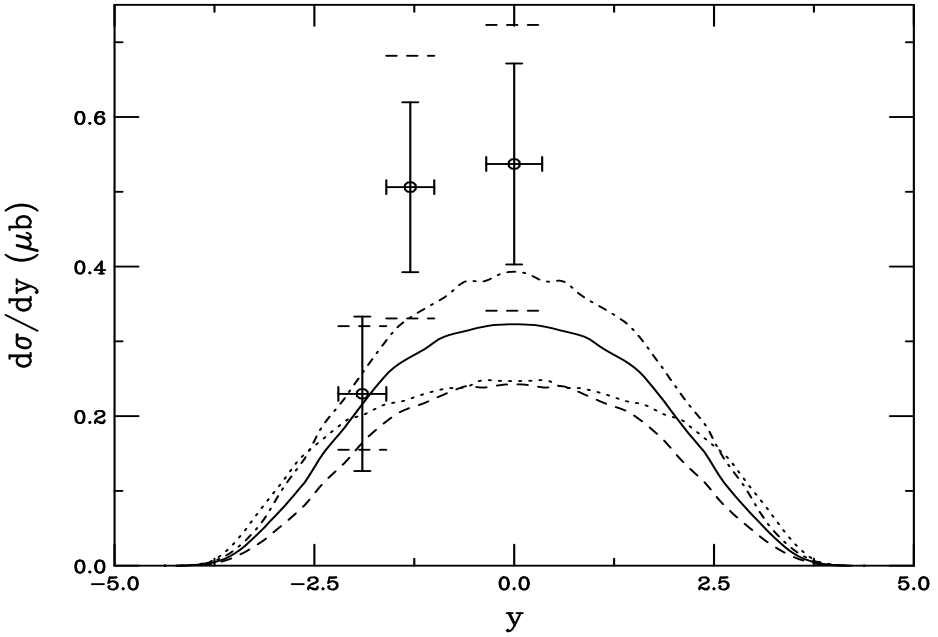

Figure 19: Direct J/ψ rapidity distributions compared to PHENIX data from Quark Matter '02. The data points are scaled to remove the $J/\psi \to l^+l^-$ branching ratio and to include direct production only. The solid curve employs the MRST HO distributions with $m = \mu/2 = 1.2$ GeV, the dashed, MRST HO with $m = \mu = 1.4$ GeV, the dot-dashed, CTEQ 5M with $m = \mu/2 = 1.2$ GeV, and the dotted, GRV 98 HO with $m = \mu = 1.3$ GeV.

Charmonium Production in the Color Evaporation Model (CEM)

Gavai *et al.*, G. Schuler and R.V.

All charmonium states are treated like $c\bar{c}$ below $D\overline{D}$ threshold

Distributions for all charmonium family members identical

At LO, $gg \to c\bar{c}$ and $q\bar{q} \to c\bar{c}$; NLO add $gq \to c\bar{c}q$

$$\sigma_C^{\rm CEM} = F_C \sum_{i,j} \int_{4m^2}^{4m_D^2} d\hat{s} \int dx_1 dx_2 \; f_{i/p}(x_1,\mu^2) \; f_{j/p}(x_2,\mu^2) \; \hat{\sigma}_{ij}(\hat{s}) \; \delta(\hat{s} - x_1 x_2 s)$$

F_C fixed at NLO

Data and branching ratios can be used to separate out the F_C's for each state in quarkonium family

Values of m and μ^2 for several parton densities fixed from $c\bar{c}$ production

J/ψ Production Cross Sections vs. Forward Data

Forward J/ψ cross sections compared to data

Inclusive J/ψ cross section–all figures include feeddown from χ_c and ψ'

Same parameters used as those that agree with $c\bar{c}$ total cross sections

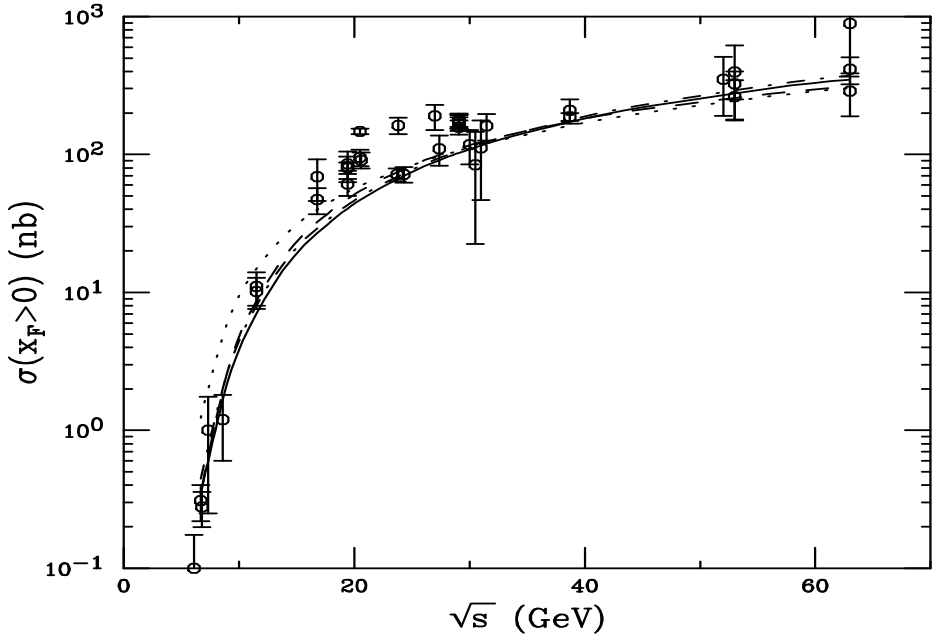

Figure 20: J/ψ production data on total cross sections with $x_F > 0$ compared to NLO CEM calculations. The solid curve employs the MRST HO distributions with $m = \mu/2 = 1.2$ GeV, the dashed, MRST HO with $m = \mu = 1.4$ GeV, the dot-dashed, CTEQ 5M with $m = \mu/2 = 1.2$ GeV, and the dotted, GRV 98 HO with $m = \mu = 1.3$ GeV.

J/ψ Production Cross Sections at $y = 0$

Inclusive $J/\psi \to l^+l^-$ cross sections compared to data

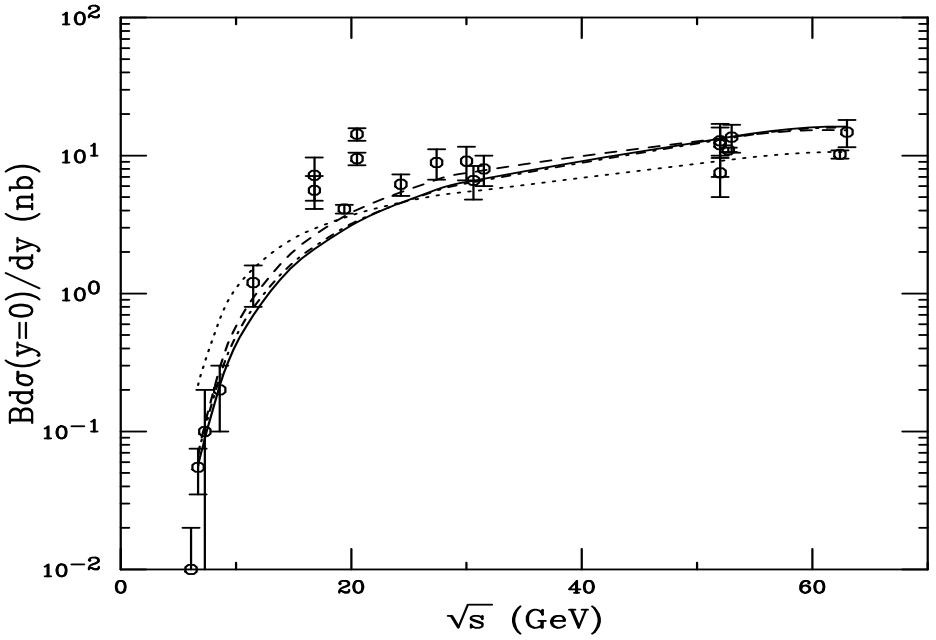

Figure 21: J/ψ production data at $y = 0$ compared to NLO CEM calculations. The solid curve employs the MRST HO distributions with $m = \mu/2 = 1.2$ GeV, the dashed, MRST HO with $m = \mu = 1.4$ GeV, the dot-dashed, CTEQ 5M with $m = \mu/2 = 1.2$ GeV, and the dotted, GRV 98 HO with $m = \mu = 1.3$ GeV.

Extrapolated J/ψ Total Cross Sections

Total forward J/ψ cross sections extrapolated to higher energy

Energy dependence obtained from NLO CEM

Factor of ~ 1.6 between results at 200 GeV

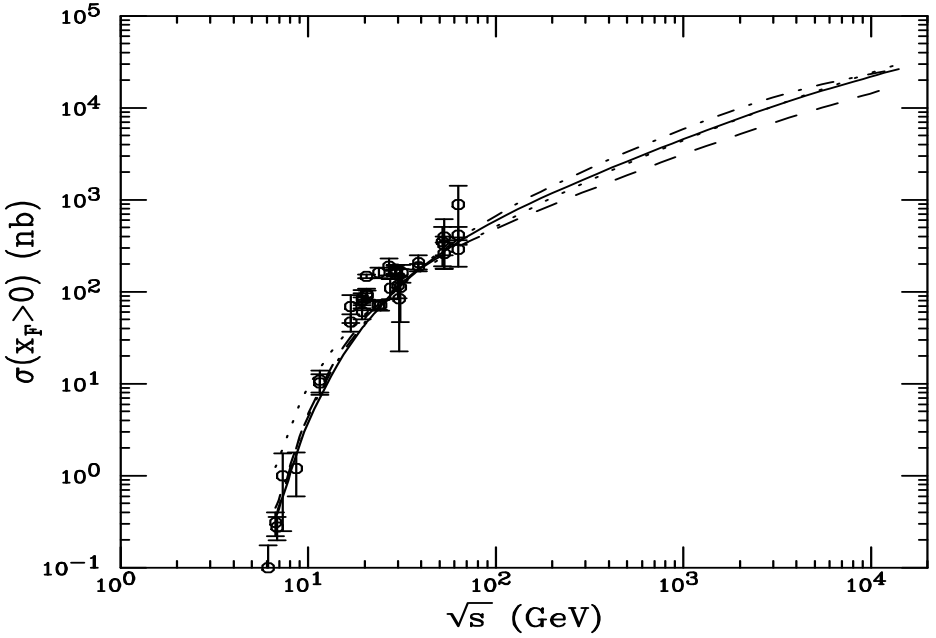

Figure 22: NLO J/ψ forward cross sections. The solid curve employs the MRST HO distributions with $m = \mu/2 = 1.2$ GeV, the dashed, MRST HO with $m = \mu = 1.4$ GeV, the dot-dashed, CTEQ 5M with $m = \mu/2 = 1.2$ GeV, and the dotted, GRV 98 HO with $m = \mu = 1.3$ GeV.

Fitted Fractions and Cross Sections for J/ψ in CEM

Case	PDF	m (GeV)	μ/m	$\sigma_{J/\psi}/\sigma_C^{\rm CEM}$
$\psi 1$	MRST HO	1.2	2	0.0144
$\psi 2$	MRST HO	1.4	1	0.0248
$\psi 3$	CTEQ 5M	1.2	2	0.0155
$\psi 4$	GRV 98 HO	1.3	1	0.0229

Table 3: The production fractions obtained from fitting the CEM cross section to the J/ψ total cross sections and $y = 0$ cross sections as a function of energy. The PDF, charm quark mass, and scales used are the same as those obtained by comparison of the $c\bar{c}$ cross section to the pp data.

Case	$\sigma_{J/\psi}^{\rm inc}$	$\sigma_{J/\psi}^{\rm dir}$	$\sigma_{\chi_{c1}}$	$\sigma_{\chi_{c2}}$	$\sigma_{\psi'}$
$\psi 1$	2.35	1.46	1.41	2.33	0.33
$\psi 2$	1.76	1.09	1.06	1.74	0.25
$\psi 3$	2.84	1.76	1.70	2.81	0.40
$\psi 4$	2.10	1.31	1.26	2.08	0.29

Table 4: The charmonium cross sections (in μb) obtained from the CEM fits for NN collisions at 200 GeV in each case. The production fractions above are them multiplied by the appropriate charmonium ratios determined from data. The inclusive and direct J/ψ cross sections are both given.

.

Extrapolated J/ψ Cross Sections at $y = 0$

Model cross sections extrapolated to RHIC energies with the preliminary PHENIX e^+e^- point at $y \sim 0$

Also shown is old Craigie parameterization, $Bd\sigma/dy|_{y=0} = 50\exp(-14.7 m_{J/\psi}/\sqrt{S})$ nb

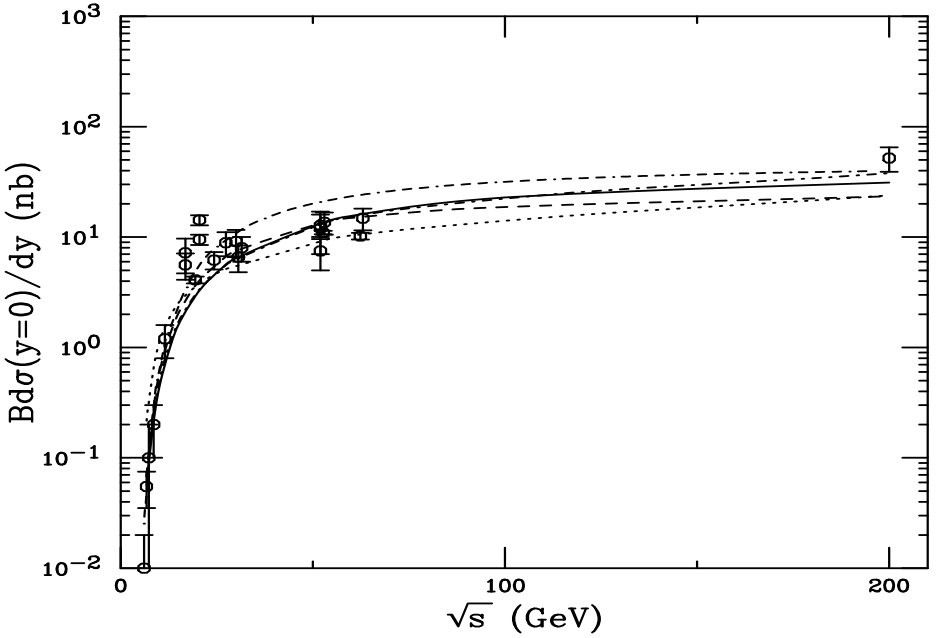

Figure 23: J/ψ production data at $y = 0$ compared to NLO CEM calculations. The solid curve employs the MRST HO distributions with $m = \mu/2 = 1.2$ GeV, the dashed, MRST HO with $m = \mu = 1.4$ GeV, the dot-dashed, CTEQ 5M with $m = \mu/2 = 1.2$ GeV, and the dotted, GRV 98 HO with $m = \mu = 1.3$ GeV. The dot-dash-dash-dashed curve is the Craigie parameterization. The PHENIX point at $y = 0$ is included.

In d+Au Interactions, Nuclear Effects Should Become Important

Nuclear effects seen to be important in charmonium production at fixed target energies

In extrapolated pA cross sections, the exponent α was shown to be a function of both x_F and p_T

Several mechanisms affect A dependence in cold matter, we consider two here:

- Nuclear Shadowing — initial-state effect on the parton distributions affecting the level of production, important as a function of rapidity/x_F
- Absorption — final-state effect, after $c\bar{c}$ that forms the J/ψ has been produced, pair breaks up in matter due to interactions with nucleons

Nuclear Shadowing

Modification of parton distributions in large nuclei measured in nuclear DIS.

Source of modification?

- Recombination of long wavelength partons
- Multiple interactions along parton path, coherence length $l_c \sim 1/2mx$

Neither can explain effect over all x.

Spatial dependence of shadowing? Partons near nuclear surface should feel weaker shadowing effect:

- Lower probability for recombination
- Reduced path length in matter near surface

Form of spatial dependence?

- If recombination or $l_c < R_A$, shadowing proportional to local nuclear density.
- If $l_c > R_A$, shadowing proportional to parton path through nucleus.

Nuclear Parton Distributions

Nuclear parton densities

$$F_i^A(x,Q^2,\vec{r},z) = \rho_A(s) S^i(A,x,Q^2,\vec{r},z) f_i^N(x,Q^2) s = \sqrt{b^2+z^2}$$
$$\rho_A(s) = \rho_0 \frac{1+\omega(s/R_A)^2}{1+\exp[(s-R_A)/d]}$$

We use EKS98 and recent Frankfurt, Guzey and Strickman (FGS) parameterization

With no nuclear modifications, $S^i(A,x,Q^2,\vec{r},z) \equiv 1$.

Spatial dependence of shadowing

Proportional to local nuclear density:

$$S^i_{\rm WS} = S^i(A,x,Q^2,\vec{r},z) = 1 + N_{\rm WS}[S^i(A,x,Q^2)-1]\frac{\rho(s)}{\rho_0}$$

Proportional to nuclear path length:

$$S^i_\rho(A,x,Q^2,\vec{r},z) = 1 + N_\rho(S^i(A,x,Q^2)-1)\int dz \rho_A(\vec{r},z)\ .$$

Normalization: $(1/A)\int d^2r dz \rho_A(s) S^i_{\rm WS,R} \equiv S^i$. Larger than average modifications for $b=0$. Nucleons like free protons when $s \gg R_A$.

Comparing Shadowing Parameterizations

Recent parameterization by Frankfurt *et al* also shown, uses EKS98 for valence shadowing, stronger gluon shadowing at low x, cuts off modification above $x = 0.25$ for sea, 0.03 for gluon

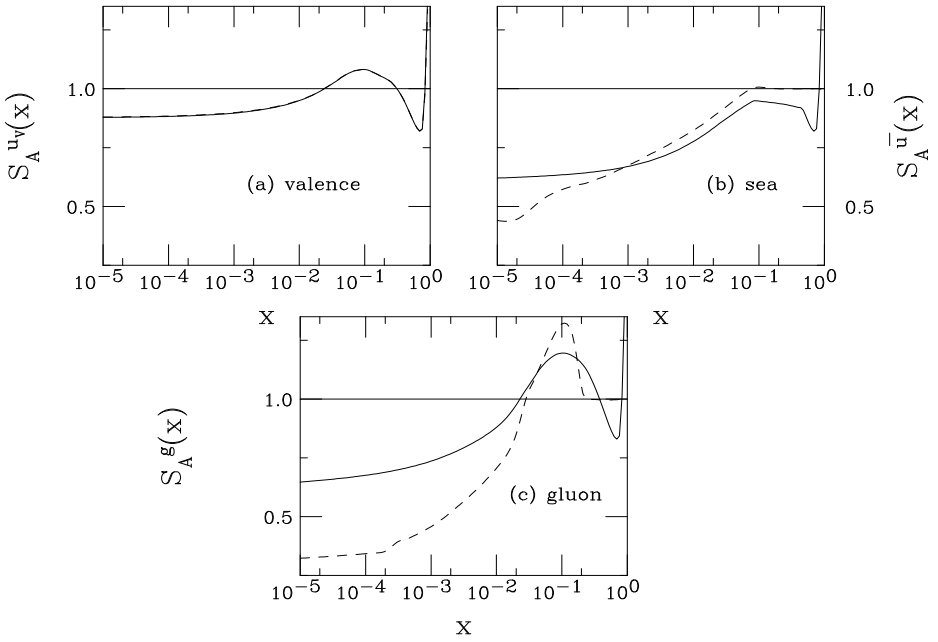

Figure 24: The EKS98 and FGS shadowing parameterizations are compared at the scale $\mu = 2m = 2.4$ GeV. The solid curves are the EKS98 parameterization, the dashed, FGS.

Effect on J/ψ pAu/pp Ratios

Ratios at LO with MRST LO PDFs and the NLO ratios with MRST HO PDFs give similar results

Frankfurt *et al* parameterization has a bigger effect at large rapidity

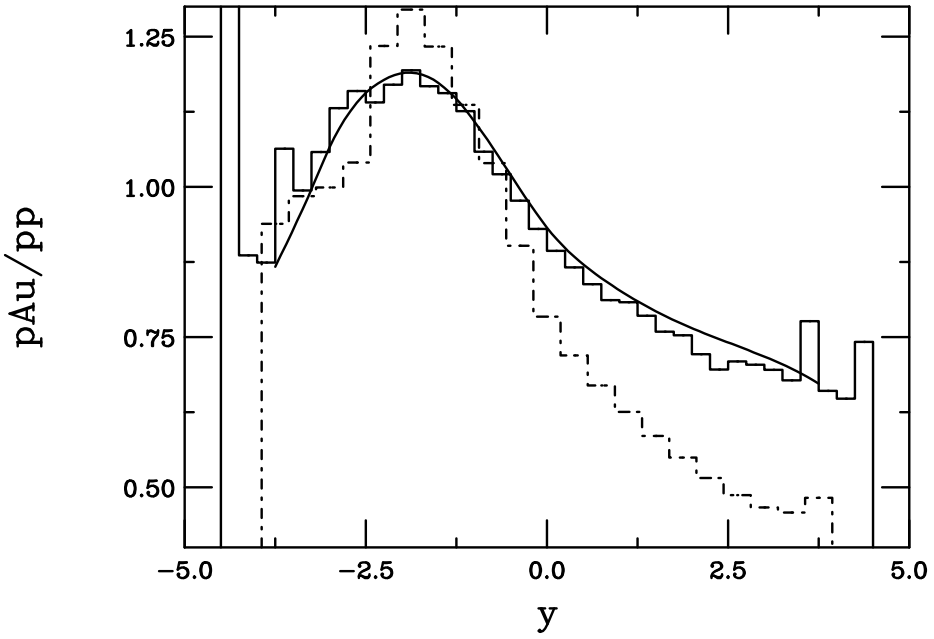

Figure 25: The J/ψ pAu/pp ratio at 200 GeV at NLO (solid histogram, using the MRST HO distributions with $m = \mu/2 = 1.2$ GeV), at LO (solid curve using the MRST LO distributions with the same mass and scale) calculated with the EKS98 parameterization are compared. The ratio with the same parameters and the FGS shadowing parameterization is given in the dashed histogram.

Inhomogeneous Shadowing in pAu, $|y| < 0.35$

Proton treated as a point, only the nuclear shape of Au included

Shadowing effect disappears at $b \sim 1.2R_A$

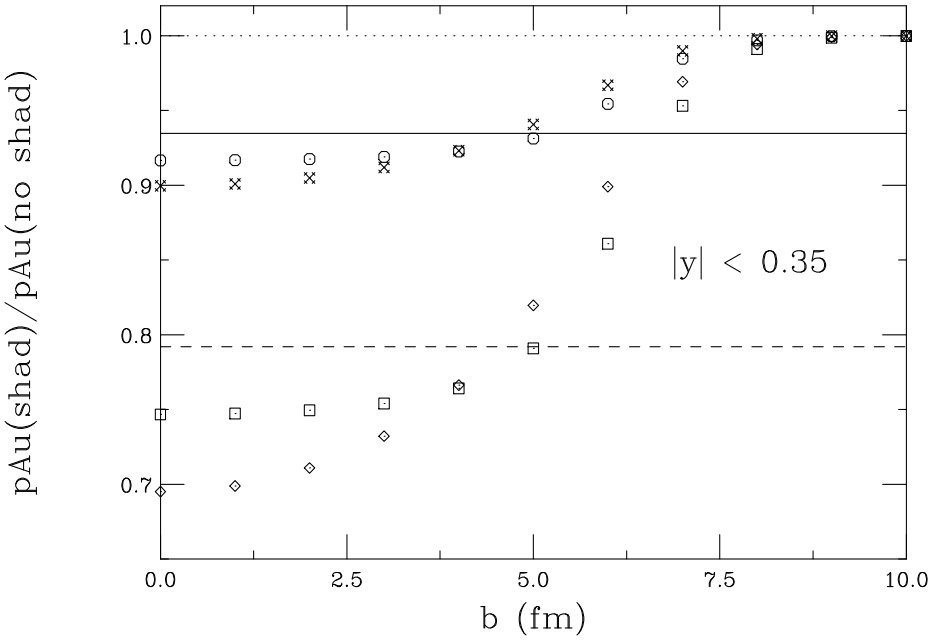

Figure 26: The J/ψ pAu/pp ratio at 200 GeV as a function of impact parameter. The results are shown for the EKS98 (solid line for homogeneous shadowing, circles and x's for inhomogeneous shadowing assuming local density and nuclear path length respectively) and FGS (dashed line for homogeneous shadowing, squares and diamonds for inhomogeneous shadowing assuming local density and nuclear path length respectively). The calculation is at LO with the MRST LO parton densities, $m = \mu/2 = 1.2$ GeV.

Inhomogeneous Shadowing in dAu, $|y| < 0.35$

Deuteron isospin included, Huthen wavefunction used

Shadowing effect does not completely die out at large *b* due to long tail of deuteron wavefunction, nuclear density of Au dies out faster with *r*

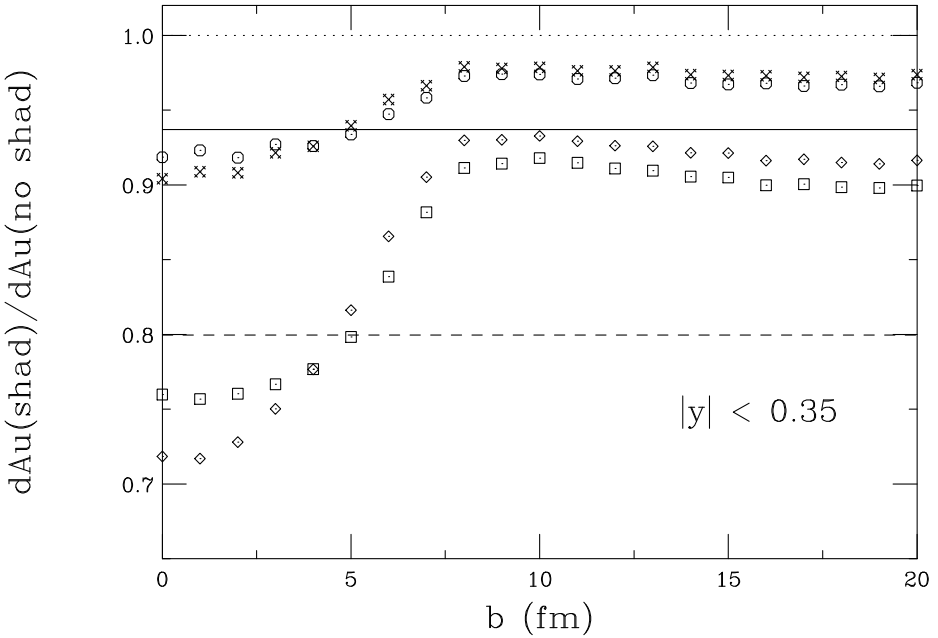

Figure 27: The J/ψ dAu/pp ratio at 200 GeV as a function of impact parameter. The results are shown for the EKS98 (solid line for homogeneous shadowing, circles and x's for inhomogeneous shadowing assuming local density and nuclear path length respectively) and FGS (dashed line for homogeneous shadowing, squares and diamonds for inhomogeneous shadowing assuming local density and nuclear path length respectively). The calculation is at LO with the MRST LO parton densities, $m = \mu/2 = 1.2$ GeV.

Comparison of Inhomogeneous Shadowing in pAu, dAu, and Au+Au

Use the local density parameterization of inhomogeneous shadowing and EKS98 to make clearer comparison

Homogeneous pAu and dAu shadowing differ by less than 1%, inhomogeneous difference significant

Stronger shadowing for Au+Au but slower growth with b

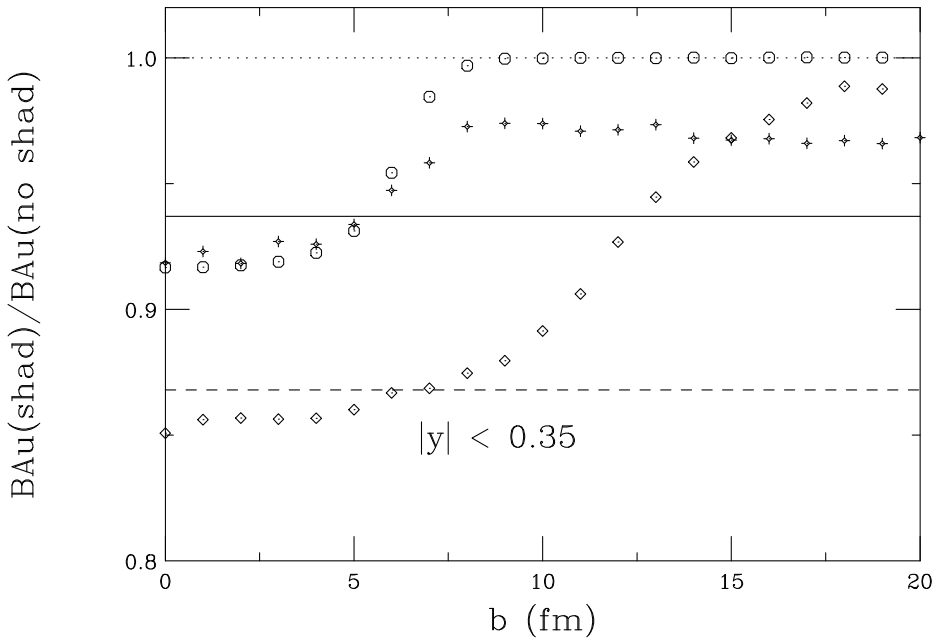

Figure 28: The J/ψ ratios in pAu, dAu and Au+Au with and without shadowing at 200 GeV as a function of impact parameter. The solid line gives the homogeneous results for pAu and dAu, the dashed is the homogeneous Au+Au result. The inhomogeneous results are shown by circles (pAu), pluses (dAu) and diamonds (Au+Au). The calculation is at LO with the MRST LO parton densities, $m = \mu/2 = 1.2$ GeV.

Rapidity Dependence in pAu, 4 b Bins

Note stronger shadowing for central impact parameters, no shadowing effect for $1.9 < b/R_A < 2.1$

Results for all b equivalent to homogeneous shadowing

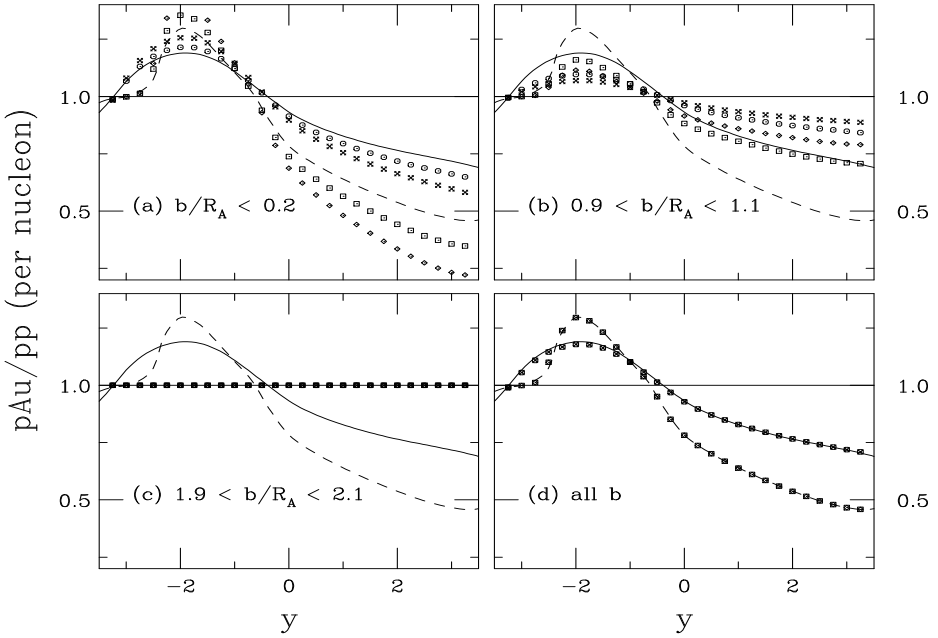

Figure 29: The J/ψ pAu/pp ratio at 200 GeV as a function of rapidity. The results are shown for the EKS98 (solid line for homogeneous shadowing, circles and x's for inhomogeneous shadowing assuming local density and nuclear path length respectively) and FGS (dashed line for homogeneous shadowing, squares and diamonds for inhomogeneous shadowing assuming local density and nuclear path length respectively). The calculation is at LO with the MRST LO parton densities, $m = \mu/2 = 1.2$ GeV. The bins are (a) $b/R_A < 0.2$, (b) $0.9 < b/R_A < 1.1$, (c) $1.9 < b/R_A < 2.1$ and (d) all b.

Rapidity Dependence in dAu, 4 b Bins

Weaker impact parameter dependence for dAu relative to pAu

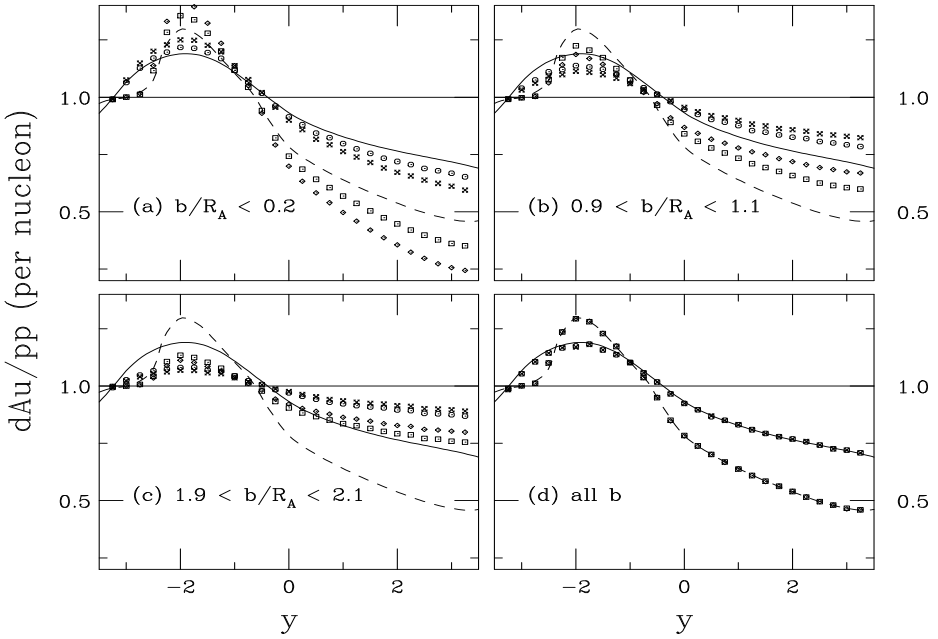

Figure 30: The J/ψ dAu/pp ratio at 200 GeV as a function of rapidity. The results are shown for the EKS98 (solid line for homogeneous shadowing, circles and x's for inhomogeneous shadowing assuming local density and nuclear path length respectively) and FGS (dashed line for homogeneous shadowing, squares and diamonds for inhomogeneous shadowing assuming local density and nuclear path length respectively). The calculation is at LO with the MRST LO parton densities, $m = \mu/2 = 1.2$ GeV. The bins are (a) $b/R_A < 0.2$, (b) $0.9 < b/R_A < 1.1$, (c) $1.9 < b/R_A < 2.1$ and (d) all b.

Effect Sizable in Central/Peripheral Ratio

Largest effect for FGS than EKS98

Path length assumption gives larger central/peripheral effect

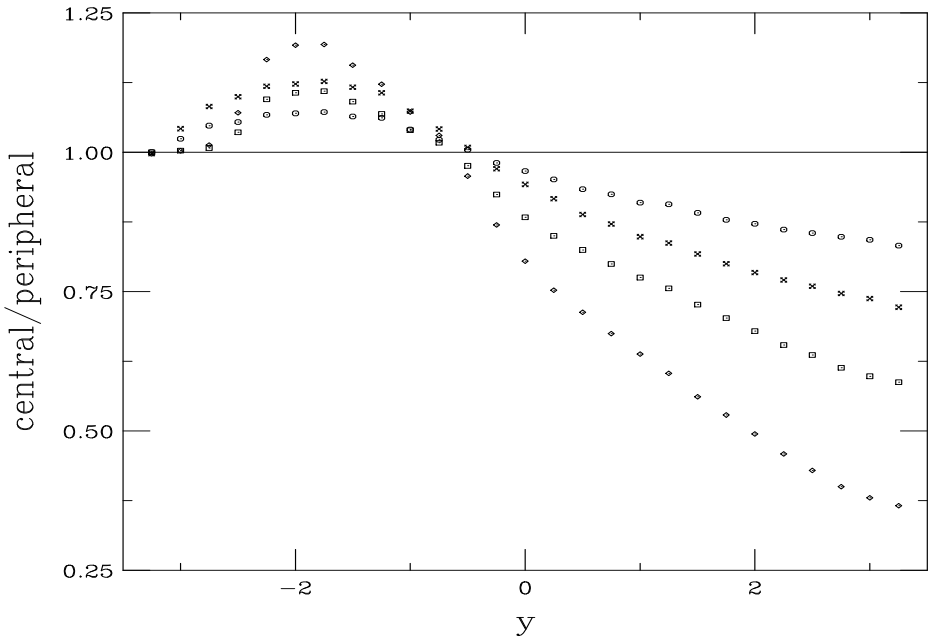

Figure 31: The J/ψ inhomogeneous shadowing ratio in central ($b/R_A < 0.2$) vs. peripheral ($0.9 < b/R_A < 1.1$) at 200 GeV as a function of rapidity. The results are shown for the EKS98 (circles and x's for local density and nuclear path length respectively) and FGS (squares and diamonds for local density and nuclear path length respectively).

PHENIX J/ψ Data Show Modification of Nuclear PDFs

Not much effect at midrapidity

Suppression seen at forward η

Nuclear shadowing alone gives fair agreement with data

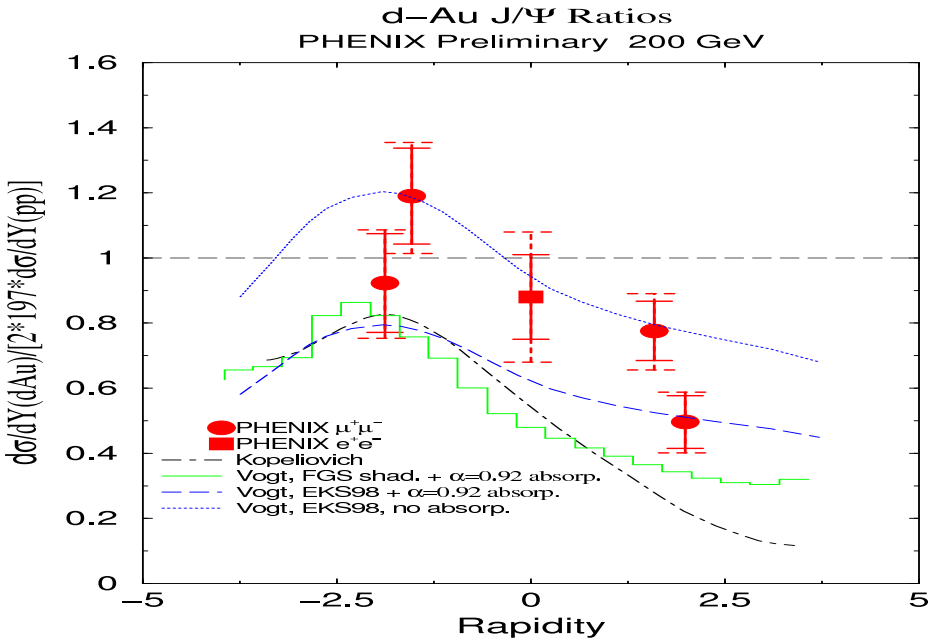

Figure 32: PHENIX d+Au/*pp* ratio for J/ψ production as a function of rapidity. The curves are theory calculations. The upper curve is EKS98 shadowing with no absorption. The lower shadowing curves have nuclear absorption added in by scaling the shadowing curves by A^{α} with $\alpha = 0.92$. [From PHENIX Collaboration, QM'04 proceedings.]

J/ψ Absorption by Nucleons

Woods-Saxon nuclear density profiles typically used

$$\begin{aligned}\sigma_{pA} &= \sigma_{pN}\int d^2b\int_{-\infty}^{\infty} dz\,\rho_A(b,z)S_A^{\rm abs}(b)\\ &= \sigma_{pN}\int d^2b\int_{-\infty}^{\infty} dz\,\rho_A(b,z)\exp\left\{-\int_z^{\infty} dz'\rho_A(b,z')\sigma_{\rm abs}(z'-z)\right\}\end{aligned}$$

Note that if $\rho_A = \rho_0$, $\alpha = 1 - 9\sigma_{\rm abs}/(16\pi r_0^2)$

We discuss absorption of color singlet and color octet states in the CEM and a combination of the two in NRQCD

Singlet Absorption Model

All $c\bar{c}$ pairs assumed to be produced in small color singlet states

Assume quadratic growth of cross section with proper time until formation time τ_F (Blaizot and Ollitrault)

Strongest at low to negative x_F where J/ψ can form in the target

Asymptotic ψ' and χ_c cross sections proportional to the final state meson size, *e.g.* $\sigma^s_{\psi' N} = \sigma^s_{J/\psi N}(r_{\psi'}/r_{J/\psi})^2$ (Povh and Hüfner)

$$\sigma_{\rm abs}(z'-z) = \begin{cases} \sigma^s_{CN}\left(\dfrac{\tau}{\tau^C_F}\right)^2 & \text{if } \tau < \tau^C_F \\ \sigma^s_{CN} & \text{otherwise} \end{cases} .$$

$$\begin{aligned} \tau^{J/\psi}_F &= 0.92 \text{ fm} \quad \sigma^s_{J/\psi N} \sim 2.5 \text{ mb} \\ \tau^{\psi'}_F &= 1.5 \text{ fm} \quad \sigma^s_{\psi' N} = 3.7\,\sigma^s_{J/\psi N} \\ \tau^{\chi_c}_F &= 2 \text{ fm} \quad \sigma^s_{\chi_c N} = 2.4\,\sigma^s_{J/\psi N} \end{aligned}$$

A Dependence of 'Color Transparency'

All states produced outside target for $x_F \geq 0$ at 920 GeV (no absorption)

Strong decrease at negative x_F expected in this model for all states but need high statistics to distinguish between them

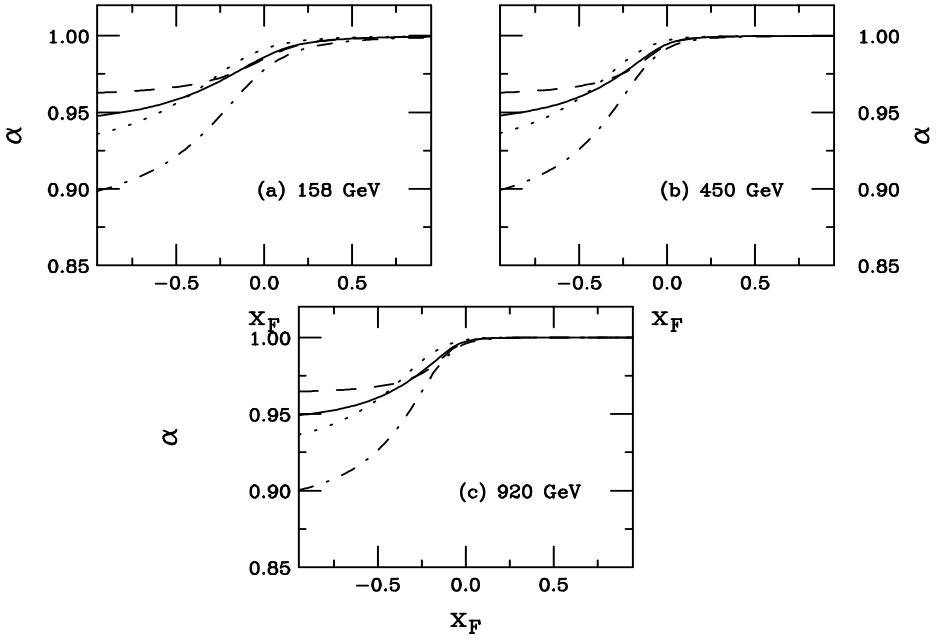

Figure 33: The *A* dependence of singlet absorption is shown for 158 (a), 450 (b), and 920 (c) GeV interactions. The total J/ψ (solid), direct J/ψ (dashed), ψ' (dot-dashed) and χ_c (dotted) dependencies are shown. [From R.V., Nucl. Phys. **A700** (2002) 539.]

Octet Absorption Model

Pre-resonant $c\bar{c}$ pairs travel through the nucleus as $|(c\bar{c})_8 g\rangle$ color octet states

Characteristic octet lifetime $\tau_8 \sim 0.25$ fm

For $x_F \geq -0.1$, path length of $|(c\bar{c})_8 g\rangle$ through the target from its production point is greater than maximum path length

These fast states pass through nucleus in color octets so that the pre-resonant A dependence is the same for J/ψ, ψ' and χ_c (Kharzeev and Satz) —$\sigma^{\,o}_{abs} = 3$ mb agrees with E866 forward A dependence

Universal constant absorption cross section usually assumed for nuclear collision studies (NA38, NA50) where $0 < x_F < 0.18$

At negative x_F, path length is shorter and octet state can neutralize its color inside target and be absorbed as color singlet

Only J/ψ likely to be fully formed inside target even though color neutralization may occur for all states

A Dependence of Octet Absorption

Dependencies different at large negative x_F where neutralization occurs

All values of α identical when state passes through target as octet

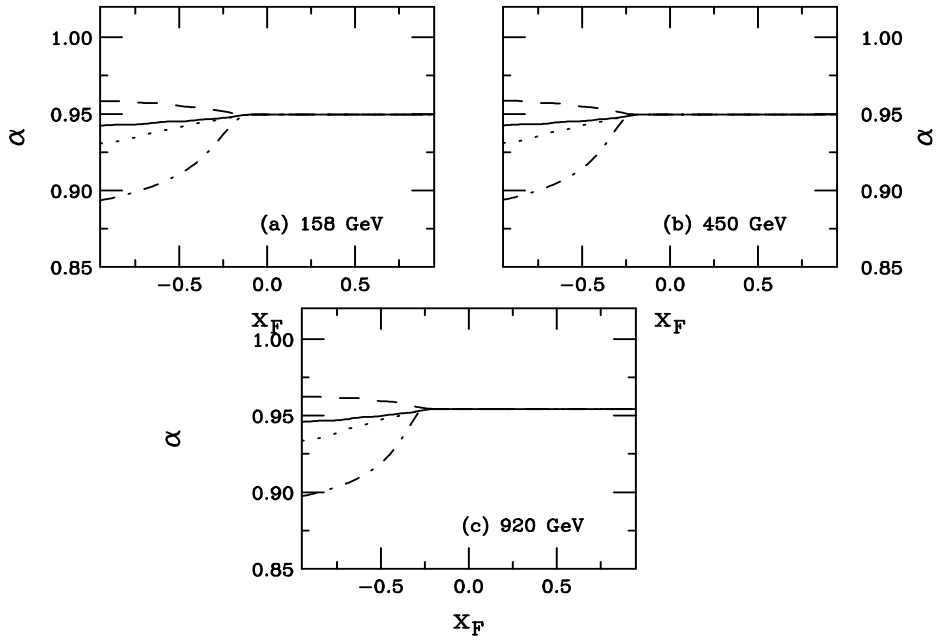

Figure 34: The A dependence of octet absorption at 158 (a), 450 (b), and 920 (c) GeV interactions. The total J/ψ (solid), direct J/ψ (dashed), ψ' (dot-dashed) and χ_c (dotted) dependencies are shown. [From R.V., Nucl. Phys. **A700** (2002) 539.]

Singlet + Octet Absorption

Relative contributions of singlet and octet production set by NRQCD (Zhang *et al.*)

Equal absorption cross sections for all octet states

Singlet cross sections set by final state size

$$\frac{d\sigma_{pA}^{\psi}}{dx_F} = \int d^2b \left[\frac{d\sigma_{pp}^{\psi,\mathrm{oct}}}{dx_F} T_A^{\psi,\mathrm{eff\,(oct)}}(b) + \frac{d\sigma_{pp}^{\psi,\mathrm{sing}}}{dx_F} T_A^{\psi,\mathrm{eff\,(sing)}}(b) \right],$$

$$\frac{d\sigma_{pA}^{\chi_{cJ}\to J/\psi X}}{dx_F} = \int d^2b \sum_{J=0}^{2} B(\chi_{cJ} \to J/\psi X) \left[\frac{d\sigma_{pp}^{\chi_{cJ},\mathrm{oct}}}{dx_F} T_A^{\chi_{cJ},\mathrm{eff\,(oct)}}(b) + \frac{d\sigma_{pp}^{\chi_{cJ},\mathrm{sing}}}{dx_F} T_A^{\chi_{cJ},\mathrm{eff\,(sing)}}(b) \right],$$

$$\begin{aligned}
\frac{d\sigma_{pA}^{J/\psi,\mathrm{tot}}}{dx_F} = \int d^2b \Bigg\{ & \left[\frac{d\sigma_{pp}^{J/\psi,\mathrm{dir,oct}}}{dx_F} T_A^{J/\psi,\mathrm{eff\,(oct)}}(b) \right. \\
& \left. + \sum_{J=0}^{2} B(\chi_{cJ} \to J/\psi X) \frac{d\sigma_{pp}^{\chi_{cJ},\mathrm{oct}}}{dx_F} T_A^{\chi_{cJ},\mathrm{eff\,(oct)}}(b) + B(\psi' \to \psi X) \frac{d\sigma_{pp}^{\psi',\mathrm{oct}}}{dx_F} T_A^{\chi_{cJ},\mathrm{eff\,(oct)}}(b) \right] \\
& + \left[\frac{d\sigma_{pp}^{J/\psi,\mathrm{dir,sing}}}{dx_F} T_A^{J/\psi,\mathrm{dir,eff\,(sing)}}(b) + \sum_{J=0}^{2} B(\chi_{cJ} \to \psi X) \frac{d\sigma_{pp}^{\chi_{cJ},\mathrm{sing}}}{dx_F} T_A^{\chi_{cJ},\mathrm{eff\,(sing)}}(b) \right. \\
& \left. + B(\psi' \to \psi X) \frac{d\sigma_{pp}^{\psi',\mathrm{sing}}}{dx_F} T_A^{\psi',\mathrm{eff\,(sing)}}(b) \right] \Bigg\}
\end{aligned}$$

$$T_A^{\mathrm{eff}}(b) = \int_{-\infty}^{\infty} dz\, \rho_A(b,z) \exp\left\{ -\int_z^{\infty} dz' \rho_A(b,z') \sigma_{\mathrm{abs}}(z'-z) \right\}$$

A Dependence of Combination Model

Total J/ψ and ψ' A dependence very similar for $0 < x_F < 0.5$ (previously measured region)

Strong octet component of direct J/ψ makes α nearly constant

Singlet contribution to χ_c means $\alpha \sim 1$ for $0 < x_F < 0.5$

$\alpha(x_F)$ depends on relative octet/singlet contributions

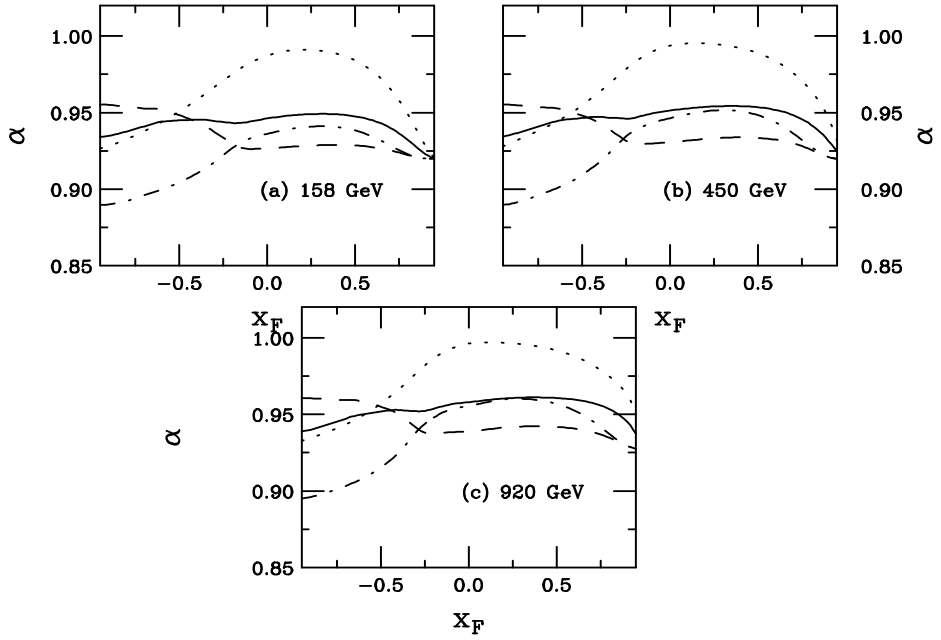

Figure 35: The A dependence of singlet and octet absorption is shown at 158 (a), 450 (b), and 920 (c) GeV. The total J/ψ (solid), direct J/ψ (dashed), ψ' (dot-dashed) and χ_c (dotted) dependencies are shown. [From R.V., Nucl. Phys. **A700** (2002) 539.]

Including Absorption with EKS98

Impact parameter averaged absorption included with homogeneous shadowing with EKS98

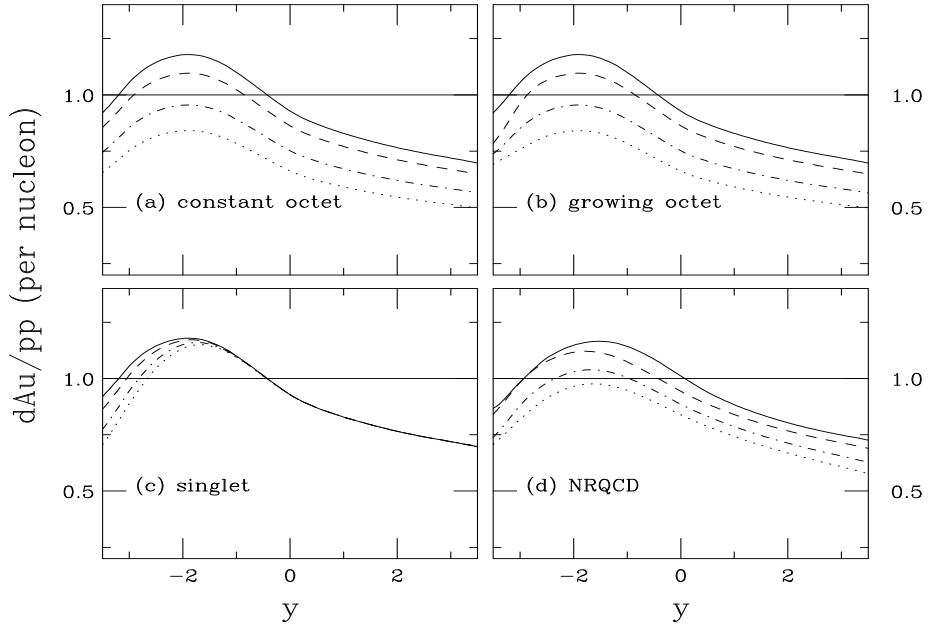

Figure 36: The J/ψ dAu/pp ratio at 200 GeV with EKS98 shadowing as a function of rapidity for (a) constant octet (assuming all states have a constant cross section and do not hadronize in the nucleus), (b) growing octet (states behave as singlets if they materialize in the medium), (c) singlet, all calculated in the CEM and (d) NRQCD with a combination of octet and singlet matrix elements. For (a)-(c), the curves are no absorption (solid), $\sigma_{abs} = 1$ (dashed), 3 (dot-dashed) and 5 mb (dotted). For (d), the results are shown for no absorption (solid, note slight difference relative to the CEM), 1 mb octet/1 mb singlet (dashed), 3 mb octet/3 mb singlet (dot-dashed), and 5 mb octet/3 mb singlet (dotted).

Including Absorption with FGS

Impact parameter averaged absorption included with homogeneous FGS shadowing

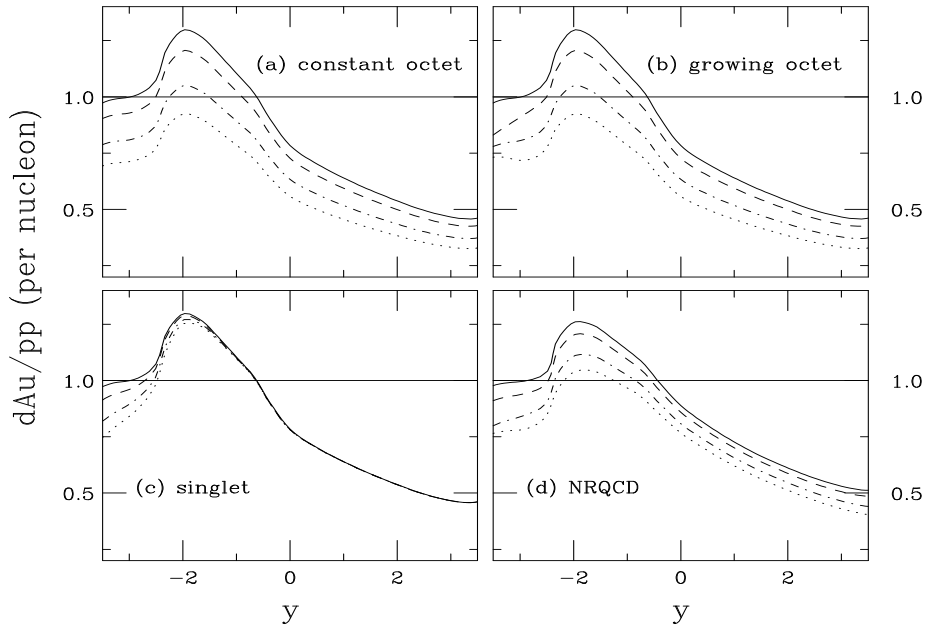

Figure 37: The J/ψ dAu/pp ratio at 200 GeV with FGS shadowing as a function of rapidity for (a) constant octet (assuming all states have a constant cross section and do not hadronize in the nucleus), (b) growing octet (states behave as singlets if they materialize in the medium), (c) singlet, all calculated in the CEM and (d) NRQCD with a combination of octet and singlet matrix elements. For (a)-(c), the curves are no absorption (solid), $\sigma_{abs} = 1$ (dashed), 3 (dot-dashed) and 5 mb (dotted). For (d), the results are shown for no absorption (solid, note slight difference relative to the CEM), 1 mb octet/1 mb singlet (dashed), 3 mb octet/3 mb singlet (dot-dashed), and 5 mb octet/3 mb singlet (dotted).

Inhomogeneous Shadowing and Absorption

$$0 < b/R_A < 0.2$$

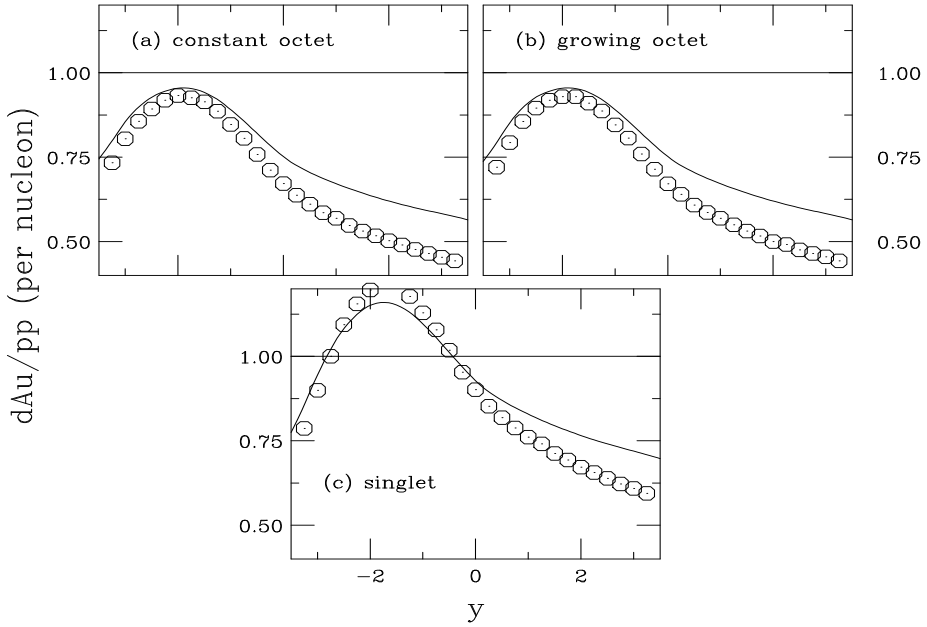

Figure 38: The J/ψ dAu/pp ratio at 200 GeV with EKS98 shadowing as a function of rapidity for (a) constant octet (assuming all states have a constant cross section and do not hadronize in the nucleus), (b) growing octet (states behave as singlets if they materialize in the medium), (c) singlet, all calculated in the CEM. The solid curves are the homogenous results while the points are impact parameter dependent shadowing and absorption.

Inhomogeneous Shadowing and Absorption

$$0.2 < b/R_A < 0.4$$

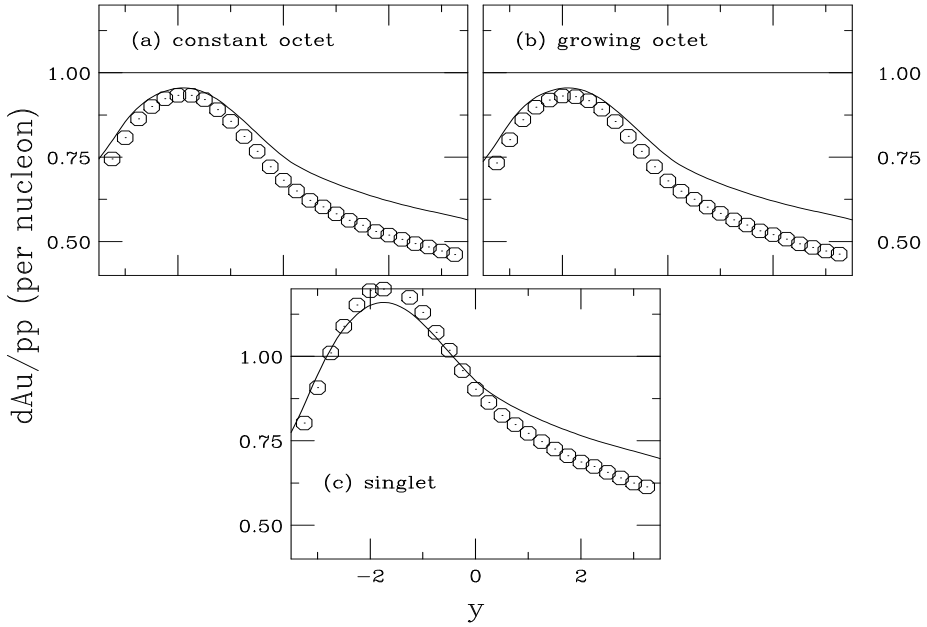

Figure 39: The J/ψ dAu/pp ratio at 200 GeV with EKS98 shadowing as a function of rapidity for (a) constant octet (assuming all states have a constant cross section and do not hadronize in the nucleus), (b) growing octet (states behave as singlets if they materialize in the medium), (c) singlet, all calculated in the CEM. The solid curves are the homogenous results while the points are impact parameter dependent shadowing and absorption.

Inhomogeneous Shadowing and Absorption

$$0.4 < b/R_A < 0.6$$

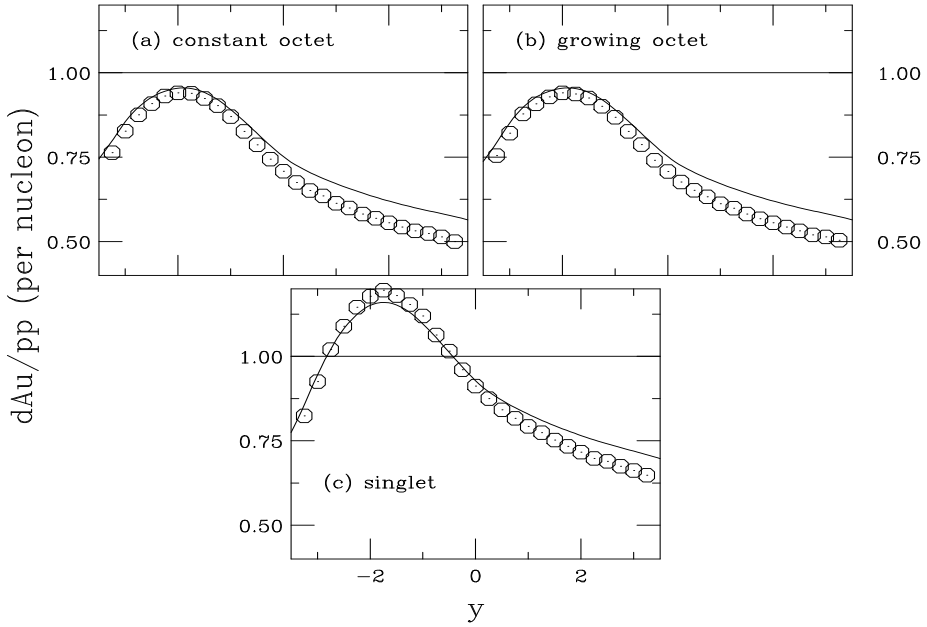

Figure 40: The J/ψ dAu/pp ratio at 200 GeV with EKS98 shadowing as a function of rapidity for (a) constant octet (assuming all states have a constant cross section and do not hadronize in the nucleus), (b) growing octet (states behave as singlets if they materialize in the medium), (c) singlet, all calculated in the CEM. The solid curves are the homogenous results while the points are impact parameter dependent shadowing and absorption.

Inhomogeneous Shadowing and Absorption

$$0.6 < b/R_A < 0.8$$

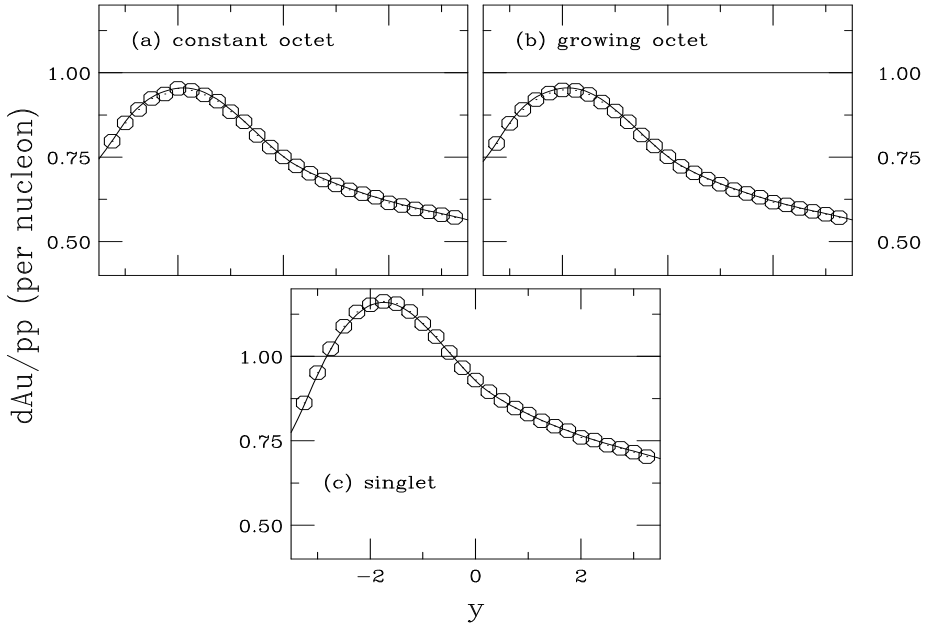

Figure 41: The J/ψ dAu/pp ratio at 200 GeV with EKS98 shadowing as a function of rapidity for (a) constant octet (assuming all states have a constant cross section and do not hadronize in the nucleus), (b) growing octet (states behave as singlets if they materialize in the medium), (c) singlet, all calculated in the CEM. The solid curves are the homogenous results while the points are impact parameter dependent shadowing and absorption.

Inhomogeneous Shadowing and Absorption

$$0.8 < b/R_A < 1.0$$

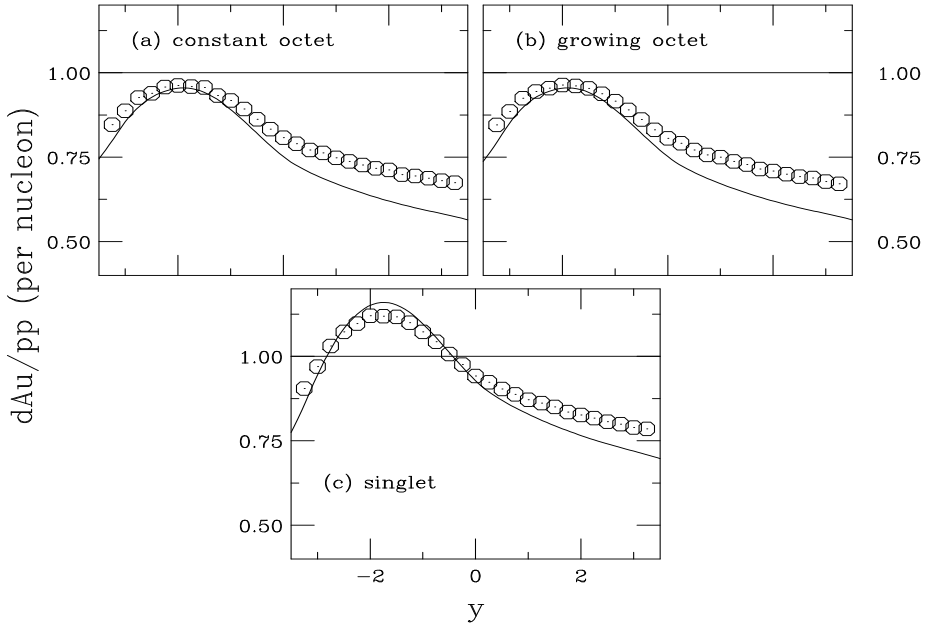

Figure 42: The J/ψ dAu/pp ratio at 200 GeV with EKS98 shadowing as a function of rapidity for (a) constant octet (assuming all states have a constant cross section and do not hadronize in the nucleus), (b) growing octet (states behave as singlets if they materialize in the medium), (c) singlet, all calculated in the CEM. The solid curves are the homogenous results while the points are impact parameter dependent shadowing and absorption.

Inhomogeneous Shadowing and Absorption

$$1.0 < b/R_A < 1.2$$

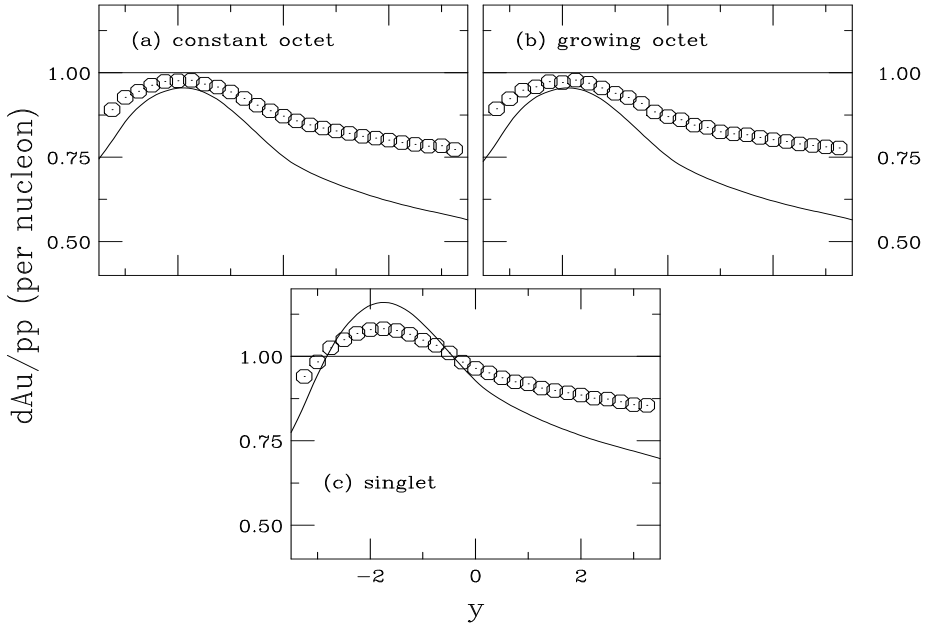

Figure 43: The J/ψ dAu/pp ratio at 200 GeV with EKS98 shadowing as a function of rapidity for (a) constant octet (assuming all states have a constant cross section and do not hadronize in the nucleus), (b) growing octet (states behave as singlets if they materialize in the medium), (c) singlet, all calculated in the CEM. The solid curves are the homogenous results while the points are impact parameter dependent shadowing and absorption.

Inhomogeneous Shadowing and Absorption

$$1.2 < b/R_A < 1.4$$

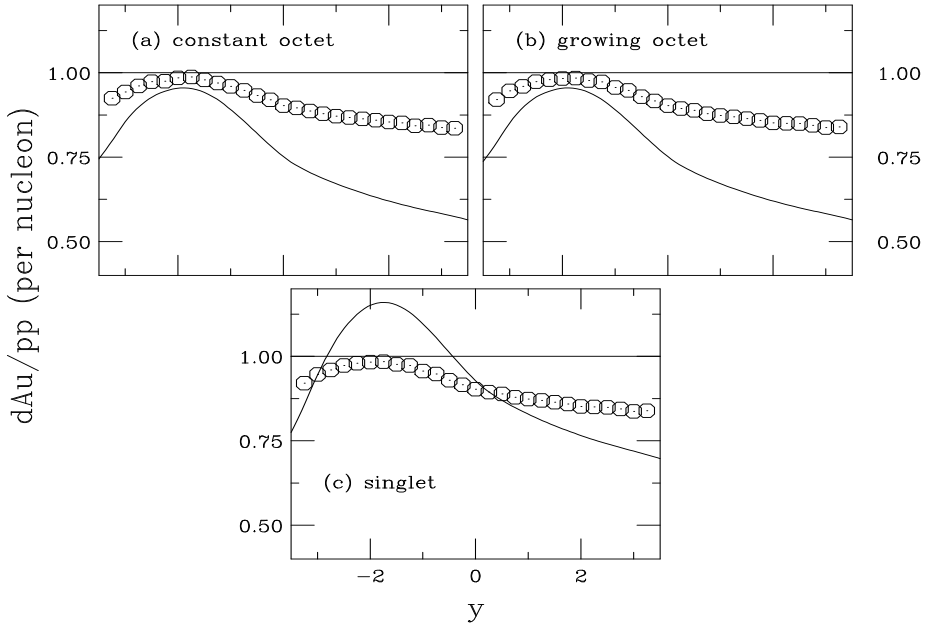

Figure 44: The J/ψ dAu/pp ratio at 200 GeV with EKS98 shadowing as a function of rapidity for (a) constant octet (assuming all states have a constant cross section and do not hadronize in the nucleus), (b) growing octet (states behave as singlets if they materialize in the medium), (c) singlet, all calculated in the CEM. The solid curves are the homogenous results while the points are impact parameter dependent shadowing and absorption.

Inhomogeneous Shadowing and Absorption

$$1.4 < b/R_A < 1.6$$

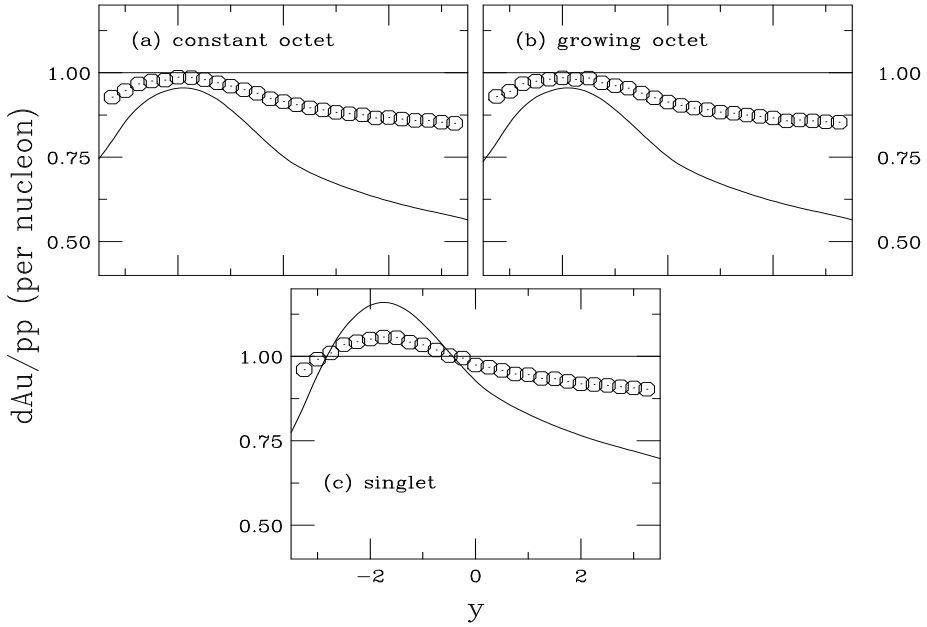

Figure 45: The J/ψ dAu/pp ratio at 200 GeV with EKS98 shadowing as a function of rapidity for (a) constant octet (assuming all states have a constant cross section and do not hadronize in the nucleus), (b) growing octet (states behave as singlets if they materialize in the medium), (c) singlet, all calculated in the CEM. The solid curves are the homogenous results while the points are impact parameter dependent shadowing and absorption.

Inhomogeneous Shadowing and Absorption

$$1.6 < b/R_A < 1.8$$

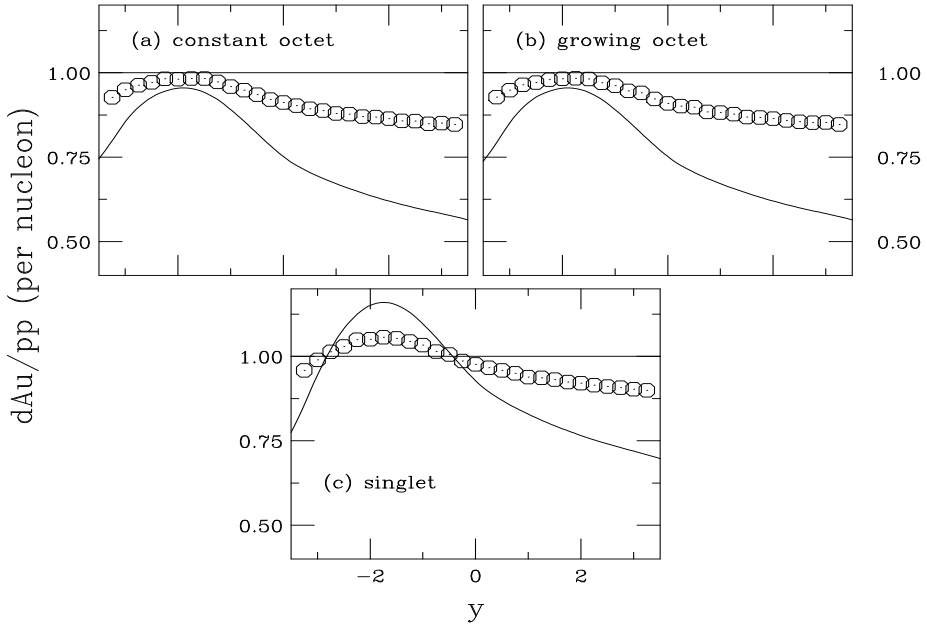

Figure 46: The J/ψ dAu/pp ratio at 200 GeV with EKS98 shadowing as a function of rapidity for (a) constant octet (assuming all states have a constant cross section and do not hadronize in the nucleus), (b) growing octet (states behave as singlets if they materialize in the medium), (c) singlet, all calculated in the CEM. The solid curves are the homogenous results while the points are impact parameter dependent shadowing and absorption.

Inhomogeneous Shadowing and Absorption

$$1.8 < b/R_A < 2.0$$

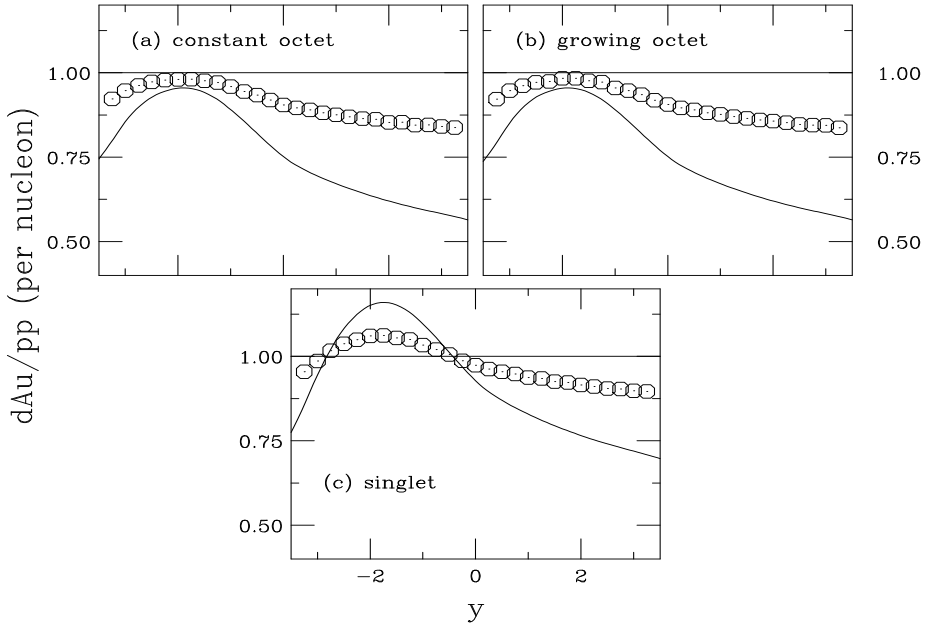

Figure 47: The J/ψ dAu/pp ratio at 200 GeV with EKS98 shadowing as a function of rapidity for (a) constant octet (assuming all states have a constant cross section and do not hadronize in the nucleus), (b) growing octet (states behave as singlets if they materialize in the medium), (c) singlet, all calculated in the CEM. The solid curves are the homogenous results while the points are impact parameter dependent shadowing and absorption.

Inhomogeneous Shadowing and Absorption

$$2.0 < b/R_A < 2.2$$

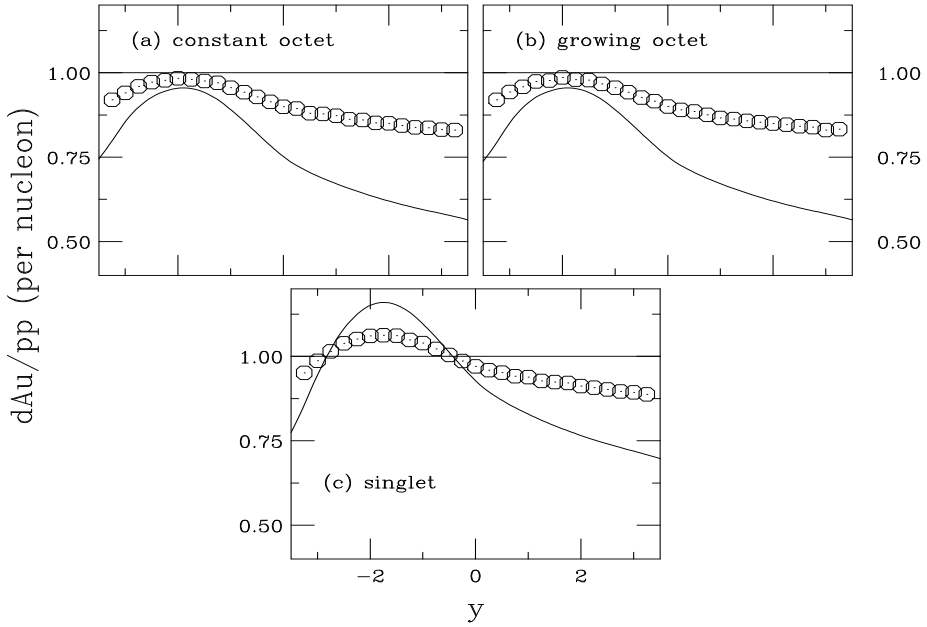

Figure 48: The J/ψ dAu/pp ratio at 200 GeV with EKS98 shadowing as a function of rapidity for (a) constant octet (assuming all states have a constant cross section and do not hadronize in the nucleus), (b) growing octet (states behave as singlets if they materialize in the medium), (c) singlet, all calculated in the CEM. The solid curves are the homogenous results while the points are impact parameter dependent shadowing and absorption.

Inhomogeneous Shadowing and Absorption

$0 < b < 20$ fm

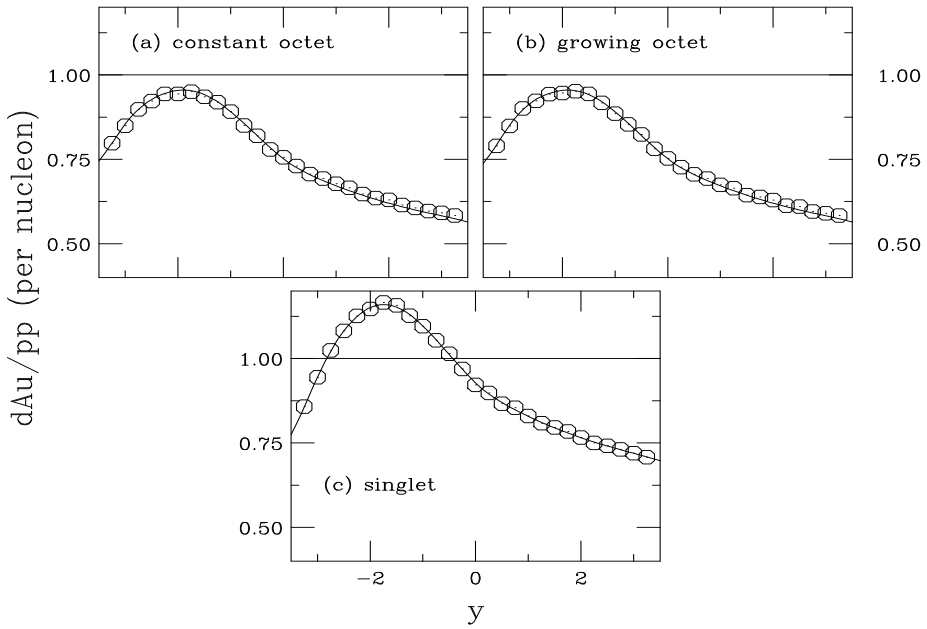

Figure 49: The J/ψ dAu/pp ratio at 200 GeV with EKS98 shadowing as a function of rapidity for (a) constant octet (assuming all states have a constant cross section and do not hadronize in the nucleus), (b) growing octet (states behave as singlets if they materialize in the medium), (c) singlet, all calculated in the CEM. The solid curves are the homogenous results while the points are impact parameter dependent shadowing and absorption.

Summary

Lots of things we don't understand yet

Why is the STAR $c\bar{c}$ cross section so big relative to other measurements?

Does fragmentation really factorize?

What is the relative importance of shadowing and absorption in J/ψ production?

How important is regeneration of J/ψ in AA?

How well can we extrapolate to higher energies?

More data will help complete this picture